Journal of Molecular Structure 1281 (2023) 135110

Contents lists available at ScienceDirect

Journal of Molecular Structure

journal homepage: www.elsevier.com/locate/molstr

Exploring the structural, photophysical and optoelectronic properties of a diaryl heptanoid curcumin derivative and identification as a SARS-CoV-2 inhibitor

Vikaraman P. Archana[a,b], Sanja J. Armaković[c,i], Stevan Armaković[d,i], Ismail Celik[e], J.B. Bhagyasree[a], K.V. Dinesh Babu[b], Mithun Rudrapal[f], Indira S. Divya[g], Renjith Raveendran Pillai[h,i,*]

[a] Department of Polymer Chemistry, Government College, Attingal, University of Kerala, Thiruvananthapuram, Kerala, India
[b] Department of Chemistry, Government College for Women, University of Kerala, Vazhuthacaud, Thiruvananthapuram, Kerala, India
[c] University of Novi Sad, Faculty of Sciences, Department of Chemistry, Biochemistry and Environmental Protection, Trg D. Obradovića 3, 21000 Novi Sad, Serbia
[d] University of Novi Sad, Faculty of Sciences, Department of Physics, Trg D. Obradovića 4, 21000 Novi Sad, Serbia
[e] Department of Pharmaceutical Chemistry, Faculty of Pharmacy, Erciyes University, Kayseri 38280, Turkey
[f] Department of Pharmaceutical Sciences, School of Biotechnology & Pharmaceutical Sciences, Vignan's Foundation for Science, Technology and Research (Deemed to be University), Vadlamudi, Guntur-522213, India
[g] Chemical Sciences and Technology Division, CSIR-National Institute for Interdisciplinary Science and Technology, Thiruvananthapuram, India
[h] Department of Physics, University College, University of Kerala, Thiruvananthapuram, Kerala, India
[i] Association for the International Development of Academic and Scientific Collaboration (AIDASCO), Novi Sad, Serbia

ARTICLE INFO

Article history:
Received 12 February 2022
Revised 3 February 2023
Accepted 5 February 2023
Available online 9 February 2023

Keywords:
Curcumin
XRD
UV–visible
DFT
Molecular dynamics
Molecular Docking

ABSTRACT

Developing modifiable natural products those having antiviral activities against SARS-CoV-2 is a key research area which is popular in current scenario of COVID pandemic. A diaryl heptanoid curcumin and its derivatives are already presenting promising candidates for anti-viral drug development. We have synthesized single crystals of a dimethylamino derivative of natural curcumin and structural characterization was done by single crystal XRD analysis. Using steady-state absorption and emission spectra and guided by complimentary ab initio calculations, we unraveled the solvent effects on the photophysical properties of the dimethyl amino curcumin derivative. Chemical reactivity of the compound has investigated using frontier molecular orbitals and molecular electrostatic potential surface. High stability of the curcumin derivative in water environment has evaluated by Radial Distributions Functions (RDF) calculated via Molecular Dynamics (MD) simulations. The inhibitory activity of the title compound was evaluated by in silico methods and the stability of the protein-ligand complexes were studied using Molecular Dynamics simulations and MM-PBSA analysis. With this detailed study, we hope to motivate scientific community to develop new curcumin derivatives against SARS-CoV-2 virus.

1. Introduction

Severe acute respiratory syndrome coronavirus 2 (SARS-CoV-2) -β sub group of Corona viruses having a genome, encapsulated by a membrane envelope infection [1] in the human host leads to COVID-19 disease, which had been declared as 6th public health emergency of international concern by World Health Organization (WHO) on January 2020. One of the effective methods for developing new drug candidates against COVID-19 is repurposing approved drugs. In recent publications the in-silico predictions- molecular dynamics simulations and molecular docking -were conducted to understand the interaction of the SARS-CoV-2 protein and its ability to act as a therapeutic agent against COVID-19 offers a path for the approved drugs to counter SARS-CoV-2 infection [2]. Along with this, researchers are actively searching for modifiable natural products which have antiviral activities. Among various natural extracts which are useful for developing drugs, curcumin and its derivatives attracted significant recognition due their wide range of pharmacological and biological applications, include antitumor [3], antifungal [4], antioxidant [5], antibacterial and antiviral [6] activities. Recently, several authors reported the effectiveness of curcumin against COVID-19 like cellular entry, replication and patho-

* Corresponding author.
E-mail address: renjithkadavoor@gmail.com (R.R. Pillai).

https://doi.org/10.1016/j.molstruc.2023.135110
0022-2860/

physiological consequences [7–10]. The polyphenol Curcumin usually exist in two tautomeric forms like diketo and keto-enol forms. The factors such as temperature and solvent characteristics determine the percentage of each tautomer [11,12] and several reports indicate that enol form predominates in solution [13–15]. It has been reported that curcumin can induce strong phototoxic reactions in micromolar concentrations because of relatively high extinction coefficient and broad absorption spectrum between 300 and 500 nm [16,17]. Because of its applicability in various fields, photophysical properties of curcumin and its derivatives have been studied widely by several authors [18–23].

Recently, Kazantzis et al. [24] synthesized some curcumin derivatives and reported that these could be useful as photosensitizers in photodynamic therapy. Among the synthetic curcumin derivatives, (1E,6E)−1,7-Bis(4-(dimethylamino)phenyl)hepta-1,6-diene-3,5–dione, was found to have increased absorption maxima and good fluorescent emission spectra and reported as a good candidate for photodynamic therapy exhibiting increased ROS generation and specific intracellular localization. Because of its attractive photophysical properties, we decided to synthesis single crystals of *(1E,6E)−1,7-Bis(4-(dimethylamino)phenyl)hepta-1,6-diene-3,5–dione* (**C–NMe$_2$**) and report its detailed crystal structure. Density Functional Theory (DFT) and Time Dependent Density Functional Theory (TDDFT) were used to study the reactive properties and photophysical properties of the synthesized compound. Applicability of title compound in the field of optoelectronics and its stability has verified using DFT and MD simulations. MD simulations revealed that the title compound is high stable in the water environment and solubility parameter has calculated to find out the suitable excipient. Though, the COVID-19 virus uses several enzymes for the replication process in the host, this replication process in the human host could be prevented by inhibiting two important enzymes, namely, Papain-Like protease (PLpro) and ADP ribose phosphatase (ADRP) [25,26]. Considering the therapeutic importance of curcumin derivatives, the inhibitory action of the title molecule on two key replication proteins of SARS-COV-2, namely Papain-Like protease (PLpro) and ADP ribose phosphatase (ADRP), was investigated using molecular docking simulations. The stability of the ligand-protein complex was further analyzed using Molecular Dynamics (MD) simulations.

2. Materials and methods

2.1. Experimental details

All materials and chemicals were of analytical grade and used as purchased without further purification. The chemicals such as p-dimethylamino benzaldehyde, acetylacetone, boron trioxide, tributyl borate, butylamine were purchased from Aldrich and S. D. Fine Chemicals, India. All the solvents used were purchased from commercial suppliers Spectrochem India, used after distillation. Synthesis of the title compound was carried out by modifying the reported procedures (Given in supplementary details). The absorption spectra were recorded in the range 200 nm-800 nm on Shimadzu UV-2550 spectrophotometer with 1.5 nm spectral bandwidth using 10 mm, 3.5 mL matched quartz cuvettes. The melting points were determined on a μThermoCal10 apparatus using thin capillary. The Fluorescence spectra were recorded using Horiba Fluorolog-3 TCSPC spectrofluorometer with 450 W xenon short arc excitation source having double-grating monochromators. The IR spectra were recorded on a Shimadzu IR prestige-21spectrometer in the range 4000–400 cm^{-1}on KBr support. The 1 H and 13C NMR spectra in $CDCl_3$ were recorded on a FTNMR (Brucker AV500) spectrometer (internal standard TMS). The mass spectra were recorded on a Thermo Scientific Exactive ESI-MS spectrophotometer. The crystal analysis of $C_{23}H_{26}N_2O_2$ was performed on BRUKER SMART APEX CCD diffractometer. A suitable crystal having approximate dimensions of 0.55 × 0.4 × 0.02 mm^3 was selected. The crystal was kept at 273.15 K during data collection. All the measurements were done with graphite monochromated Mo Kα radiation (λ = 0.71073). 6513 reflections measured (3.3° ≤ 2θ ≤ 42.996°), 2171 unique (*R*int = 0.0428, Rsigma = 0.0452) which were used in all calculations. The final R_1 was 0.0984 ($I > 2\sigma$ (I)) and wR_2 was 0.1954 (all data). All the atoms except hydrogen were refined anisotropically. Hydrogen atoms were treated with mixed method, processed with max D-A distance 2.9 Å and minimum angle 120°. Refinement details are given in the supporting information. The structure was solved using Olex2, the structure solution program using Charge Flipping and refined with the SHELXL refinement package using Least Squares minimization. Mercury software (v 3.8) is used for structure plotting.

2.2. Computational details

The Structure optimizations of Curcuminoid **C–NMe$_2$,** including β-diketone and keto-enol were performed with B3LYP functional [27–30] with 6–311 G (d, p) basis set. On the basis of ground state optimization, TDDFT calculations were performed on the keto-enol isomer of the title compound to obtain vertical excitations and solvent effects on the photophysical properties. All of the DFT calculations were performed on Gaussian 09 quantum chemistry program [31]. To confirm that the geometries are true minima, vibrational harmonic frequencies were calculated and found to be positive for all normal modes. All the ground state properties were predicted using the optimized geometry in the di-keto form. Previous studies using X-ray revealed that the enol tautomer will be dominant in solution [32]. Therefore, TDDFT calculations were performed with the optimized geometry for enol tautomer of the title compound.

Jaguar program [33,34] for DFT calculations, as implemented in the Schrodinger Materials Science Suite 2021–3, have been utilized to calculate the Molecular Electrostatic Potential (MEP), and selected optoelectronic properties. Desmond program [35], also as implemented in Schrodinger Materials Science Suite 2021–3, has been used for performing the MD simulations, using the OPLS3e force field [36–39]. Molecular dynamics (MD) simulation was performed with Gromacs 2019.2 version to examine the dynamic behavior of protein-ligand complexes [40]. The topology of the proteins was created with gromos54a7 force field [41] and SCP water model. Topology files of ligand were obtained via the GlycoBioChem PRODRG2 [42] server. Triclinic box type and simple point charge SPC was preferred for solvation at a distance of 10 Å from the protein-ligand complex. The system was neutralized by adding 0.15 M NaCl. Energy minimization was performed in 5000 steps with the steepest descent integrator. Equilibrated with NVT and NPT stages of 0.3 ns at 1atm pressure and 300 K temperature, V-rescale thermostat, and Parrinello-Rahman barostat, respectively. Molecular dynamics simulation of 1000 frames with 100 ns were performed to 2 fs. Verlet algorithm was used as the cut-off scheme, the particle-mesh Ewald (PME) algorithm was used as coulomb type and potential-shift was used as coulomb-modifier, coulomb-modifier was used as vdw-type and potential-shift was used vdw-modifier. PME method and the linear constraint (LINCS) algorithm were performed to calculate long-range electrostatic interactions and covalent bond constraints, respectively. Molecular dynamics simulations were performed under periodic boundary conditions (PBC). Trajectory analysis was done with gmx rms, rmsf, gyrate and hbond scripts. Binding free energy calculations between 80 and 100 ns were performed with g_mmpbsa [43] script according to the equation

$$\Delta G_{bind} = G_{Complex} - G_{protein} - G_{ligand}$$

Where $G_{complex}$, $G_{protein}$ and G_{ligand} are the free energies of complex, protein and ligand, respectively.

3. Results and discussion

3.1. Structure description

The title compound was synthesized from p-dimethylaminobenzaldehyde as per the previously reported procedure and were characterized on the basis of spectroscopic and single crystal evidence (Supplementary Details). In ^{1}HNMR peak at δ 3.011 (12 H) indicates the dimethyl amino groups. Peak at δ 6.67 & δ 7.60 indicates -C=CH protons and –C=CH adjacent to Oxygen atom. The $-CH_2$ protons in between the diketone moiety indicated by the peak at δ 6.424. Peak at δ 183 in ^{13}CNMR corresponds to the carbonyl carbon. Single crystal studies reveal that the compound **C–NMe2** crystallizes in monoclinic space group $P2_1/n$ with unit cell parameters of a = 13.534(3), b = 6.1145(11), and c = 23.888(4) Å, $\alpha/°$=90 $\beta/°$=96.838(4) $\gamma/°$=90. Crystal data, data collection and structure refinement details are summarized in Table 1. Thermal ellipsoid plot of the asymmetric unit with atom numbering scheme is shown in Fig. 1. Each unit cell contained four C–NMe2 molecules. The structure of the molecule may be considered as three substituted planar group interconnected through C_7–C_8 and C_{12}–C_{13}. Molecule possess inversion symmetry, with the active methylene group being located about center of inversion (C_{10}). The methylene group inclined to the phenyl ring by ~174° (C_{13} C_{12} C_{11} C_{10} =176.8(6)° and C_7 C_8 C_9 C_{10} =171.2(6)°). The three bond angles C7-C6-C1, 124.1(5); C7-C6-C5, 118.9(5); C1-C6-C5, 117.0 (5); with C6 as center, on addition gives the C–C-C bond angle value of 360.0° indicates the coplanarity of C7 with aromatic ring. C6-C7 [1.455(7) Å] and C8-C9 [1.457(8) Å] bonds are longer than C7-C8 [1.336(8) Å] and O1-C9 [1.304(7) Å] bonds. Similarly, C13-C14 [1.452(8) Å] and C12-C11 [1.455(8) Å] bond lengths are longer than C12-C13 [1.333(8) Å] and O2-C11 [1.305(7) Å] which implies the highly conjugated system. Positional parameters, relevant bond lengths, bond angles and torsional angles are included in the supplementary details.

Notably, the C–O bond distance of the carbonyl groups are found to be O1-C9 1.304(7) Å & O2-C11 1.305(7) Å, which is longer than the normal C–O bond distance in carbonyl groups (1.21 Å). This can be attributed to the extended pi-electron conjugation in the molecular structure of C–NMe_2. The derivative C–NMe_2 is designed by linking two donor (NMe_2 groups on either side)- acceptor (C = O groups) moieties, which facilitates efficient electron transfer. As a result of this conjugation electron density around the oxygen atom further increases and thus the C–O bond length also increases.

Generally in the absence of strong hydrogen bonding the weak C–H….O bonds govern the crystal packing. Here the carbonyl group act as a good C–H…O hydrogen bond acceptor and the weak intermolecular C–H….O interactions along a direction connects two molecules to form a dimer parallel to (010) plane. The C–H…O hydrogen bonding geometry of the molecule **C–NMe_2** is given in supplementary details. The D…A distance is in between the range of 2.5–3.8 Å and the angle is within the range of 110–180°. All the contacts of intermolecular interactions are also included in supplementary details. Thus, formed dimer columns are then connected by C–H….O(2.52 Å) and π… π interactions(3.386 Å) parallel to (010) plane resulting a 3D close packed structure given in Fig. 2.

Table 1
Crystal data and structure refinement of the title compound.

Identification code	C-NMe2
Empirical formula	$C_{23}H_{26}N_2O_2$
Formula weight	362.46
Temperature/K	273.15
Crystal system	monoclinic
Space group	$P2_1/n$
a/Å	13.534(3)
b/Å	6.1145(11)
c/Å	23.888(4)
$\alpha/°$	90
$\beta/°$	96.838(4)
$\gamma/°$	90
Volume/Å^3	1962.8(6)
Z	4
ρ_{calc}g/cm^3	1.227
μ/mm^{-1}	0.078
F(000)	776.0
Crystal size/mm^3	0.55 × 0.4 × 0.02
Radiation	MoKα (λ = 0.71073)
2Θ range for data collection/°	3.3 to 42.996
Index ranges	$-13 \le h \le 13$, $-6 \le k \le 5$, $-24 \le l \le 20$
Reflections collected	6513
Independent reflections	2171 [R_{int} = 0.0428, R_{sigma} = 0.0452]
Data/restraints/parameters	2171/0/264
Goodness-of-fit on F^2	1.210
Final R indexes [$I>=2\sigma$ (I)]	R_1 = 0.0984, wR_2 = 0.1890
Final R indexes [all data]	R_1 = 0.1109, wR_2 = 0.1951
Largest diff. peak/hole / e Å^{-3}	0.24/−0.31

3.2. Hirshfeld surface analysis

Crystal Explorer 17 [44] has been used to generate the Hirshfeld surfaces and the related two-dimensional fingerprint plots for the crystal structure of the title compound. This graphical method helps us to visualize and understand the intermolecular interactions within a given crystal structure. In the graphical tool used for visualizing the Hirshfeld surface, d_i and d_e represent the distance from the Hirshfeld surface to the nearest atoms, which are situated inside and outside of the surface, respectively [45,46]. In the Hirshfeld surface analysis, those regions in the crystal structure which are of particular importance is identified by mapping normalized contact distance (d_{norm}), which is expressed as

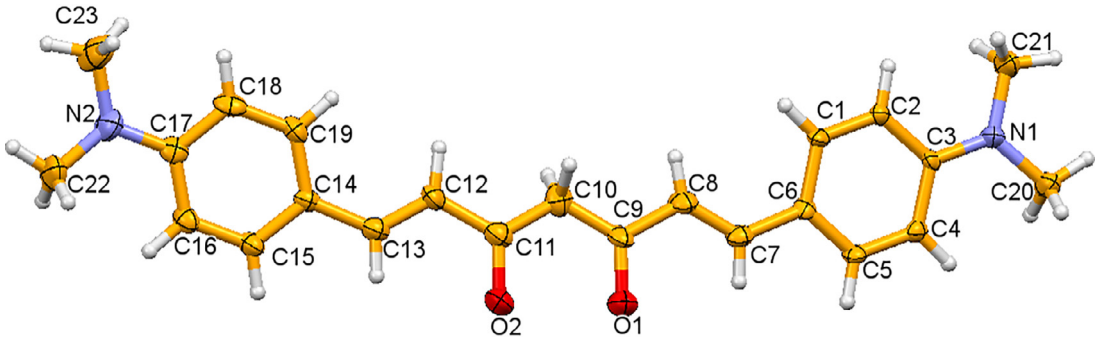

Fig. 1. Thermal ellipsoid plot of **C–NMe_2** with atom numbering scheme (40% probability factor for the thermal ellipsoids).

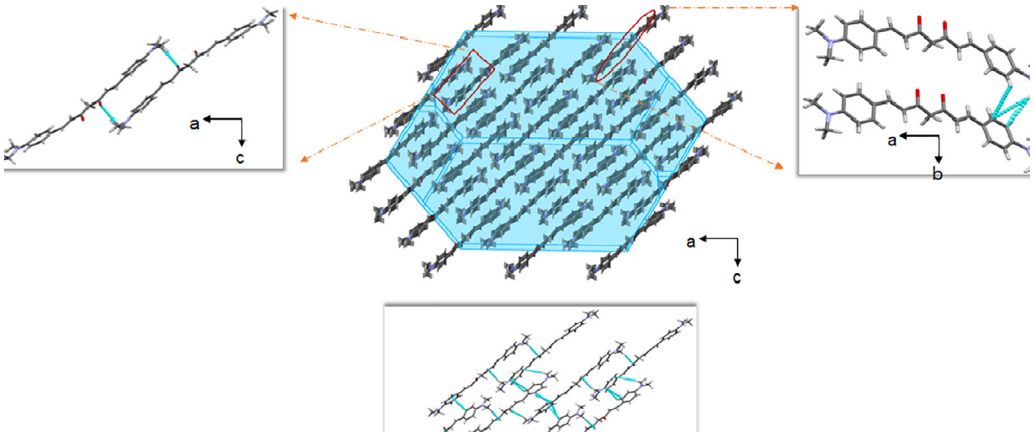

Fig. 2. Packing diagram of **C–NMe$_2$** showing the intermolecular interactions.

$d_{norm} = \frac{(d_i - r_i^{vdw})}{r_i^{vdw}} + \frac{(d_e - r_e^{vdw})}{r_e^{vdw}}$, where r_i^{vdw} and r_e^{vdw} are the van der Waals radii of the atoms in the crystal structure [47]. One of the commonly used ways of representing the Hirshfeld surfaces involves the mapping of d_{norm} values on to the Hirshfeld surface, in which interactions between the atoms in a crystal structure were quantified using a color gradient, which is very useful to illustrate the relative positioning of neighboring atoms belong to the interacting molecules graphically. In such a surface representation, red spots represent shorter and hence stronger contacts for which distance separating neighboring atoms is less than the sum of their respective van der Waals radii, blue shows longer contact for which distance separating neighboring atoms surpass the sum of their respective van der Waals radii and white gradient is for contacts which lie close to the sum of van der Waals radii of neighboring atoms which are interacting [45]. The unique 3D Hirshfeld surfaces and their 2D fingerprint maps were shown in the Figs. 3 and 4.

The presence of several red spots on the d_{norm} surface (Fig. 3a) of the title compound indicates the existence of strong C–H…O interactions within the crystal structure. The presence of adjacent red and blue triangle pair on the shape index surface (Fig. 3b) shows the evidence of π-π stacking interaction in the molecular packing of the title compound. Big red spots on both front and rear side of the shape index surface of the Hirshfeld surface indicate the presence of C–H…π interactions. The large flat region on the curvedness surface of Hirshfeld surface (Fig. 3c) confirms the presence of π-π interactions in the crystal packing structure of the title compound. The 2D fingerprint plots of the title compound given in Fig. 4, provide quantitative information about the individual contribution of the intermolecular interactions in crystal structure. In the 2D plots, different short-range interactions are shown by the blue regions and gray shade is used as the outline of the full fingerprint plots. The contribution of the H…H intermolecular interactions have the highest contribution to the total Hirshfeld surface for the crystal structure and these interaction amounts to 56.4% of the total surface area of the surface. These H…H intermolecular interactions scattered throughout the entire surface with a single broad peak at $d_i = d_e \sim 2.2$ Å. The second most frequent interactions are C…H interactions and these interactions 24.9% of the total Hirshfeld surface and scattered throughout the two-dimensional finger plots with two symmetric broad peaks with $d_i = d_e \sim 2.6$ Å. The O…H interactions with a 13.9% contribution, are present in the middle of the scattered points in the two-dimensional fingerprint plots as two symmetric sharp peaks. From the detailed analysis of crystal structure, it is evident that the interactions which play the major roles in the crystal packing are hydrogen bond and van der Waals interactions.

3.3. Photophysical properties

The dimethylamino derivative C–NMe2 showed distinct photophysical properties as compared to the traditional Curcumin. The solubility of the title compound is examined in different polar and non-polar solvents. It is observed that the dimethylamino curcuminoid (C–NMe2) derivative is readily soluble in polar solvents such as DMSO, DMF, methanol, ethanol, acetonitrile, chloroform, dichloromethane, ethyl acetate, whereas less or poor solubility in non-polar solvents such as hexane, toluene, cyclohexane etc. The molecule is insoluble in aqueous medium (pH 7.4). It exhibited good stability in common organic solvents. The UV–Visible spectrum of the synthesized derivative was recorded in different solvents (Fig. 5a). It showed a single intense absorption peak in polar protic and aprotic solvents such as methanol, ethanol, chloroform, acetonitrile, DMSO whereas in nonpolar solvents like hexane and toluene, it exhibited two peaks centered around 440 nm 460 nm. Interestingly, when solvent polarity increased from nonpolar to polar, we observed red shift in absorption. In all the solvents a red shift is observed in the absorption maximum with respect to the absorption maximum of Curcumin. The dimethylamino derivative C–NMe2 showed a red shifted absorption maximum in the range of ca. 438–503 nm whereas Curcumin showed an absorption maximum around 430 nm in polar solvents [13]. The molar extinction coefficients of the derivative were calculated in different solvents by following the Beer–Lambert Law and is found to be 8.5 × 104 M-1 cm-1 (acetonitrile), 8.6 × 104 M-1 cm-1 (chloroform), 5.2 × 104 M-1 cm-1 (methanol) etc. The solvatochromic change in the absorption spectrum of C–NMe2 was observed while going from non-polar to polar solvents., which is evident from the fact that in hexane, the absorption spectrum of C–NMe2 appears as a broad band with two peaks at 438 nm and 463 nm, whereas in DMSO, the absorption maximum observed at 503 nm. Studies on Curcumin and related compounds suggest that the π-π^* transition and the enol (*cis* or trans) form are the reason of this red shift in polar solvents [13,21,48]. The absorption spectrum of C–NMe2 in various solvents is shown Figs. 5a and 5b indicates the significant changes in the absorption spectra and absorption maxima of C–NMe2 in polar (DMSO) and non-polar (hexane) solvents.

The fluorescence properties of the derivatives were studied in different solvents and exhibited a similar shift as that of absorption spectra. In emission spectra recorded at room temperature, notably, the dimethylamino derivative C–NMe2 showed considerable red shift in emission maximum of ca. 60-90 nm when compared to its parent compound Curcumin in most of the organic solvents (Fig. 6). Interestingly, in methanol, C–NMe2 exhibit strong NIR emission with the fluorescence maximum centered at

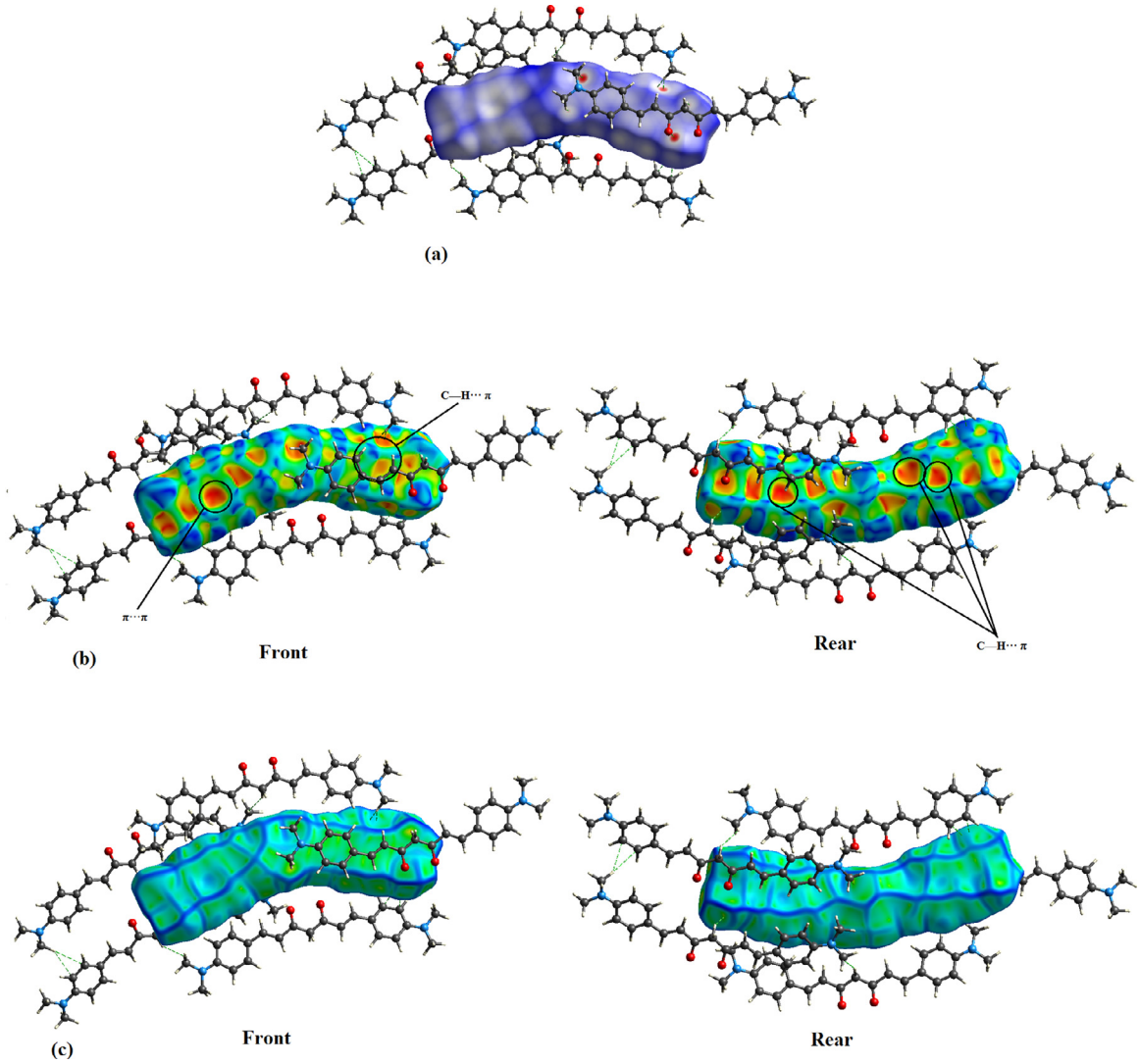

Fig. 3. Views of the Hirshfeld surface of the title compound plotted over (s) dnonrm (b) shape-index (c) curvedness.

ca. 650 nm. The large stock shift of the derivative in protonated solvents such as methanol (ca. 165 nm) suggest the probability of Excited State Intra molecular Proton Transfer (ESIPT). This phenomenon further confirms with the solvent dependent absorption and emission changes of C–NMe2. The difference in absorption and emission maximum (Stokes shift) increases as the polarity increases whereas in low polar solvent like hexane much stokes shift is not observed. In the excited state the polar solvents may facilitate the proton transfer which results large stokes shift. In order to confirm this, spectra were recorded in 77 K and room temperature also (Figure S1). It is observed that at 77 K the emission spectra of the compound in polar and nonpolar solvents were identical.

The absorption spectra of the title compound in different solvents simulated using TD-DFT is depicted in Fig. 7. In the case of title compound, theoretically stimulated spectra emulate the experimental spectra and the absorption maxima in different solvents were significantly red-shifted with respect to that of curcumin [49]. The experimental findings were reproduced by theoretical simulations and as evident from the simulated spectra, there is almost no change in the absorbance peak when the polarity of the solvent changed, except for cyclohexane, which is highly non-polar compared to others. From the analysis of UV–Visible spectra calculate in cyclohexane solvent, there is a hypsochromic shift of the absorption peak of 20 Å compared to other solvents. Also, there is a small red shift (~3 Å) of the absorption peak has observed for DMSO. On the other side, the oscillator strength is same in all solvents, which clearly indicates that nature of the solvent has little effect on the intensity of the absorption peaks. The two lowest energy excitation peaks observed around 490 nm and 320 nm in all solvents are mainly contributed by HOMO-LUMO transitions and are of $\pi \rightarrow \pi^*$ nature. The lowest excitation S0→S1 could be due to the electron transfer between the central and two opposite tail parts of the molecule.

3.4. Optoelectronic properties

The applicability of the title molecule in the field of organic electronics is evaluated by calculating parameters such as reorganization energies, charge transfer rates and charge mobility using theoretical methods. Charge transfer rates between molecules are governed by the two main parameters, reorganization energies of holes and electrons, λ and the extent to which orbitals of interacting molecules are overlapped. The latter one is described by the charge transfer integral t, which can be calculated in the framework of dimer frontier orbital splitting approximation. The famous Marcus semi-empiric approach can be used to estimate the charge

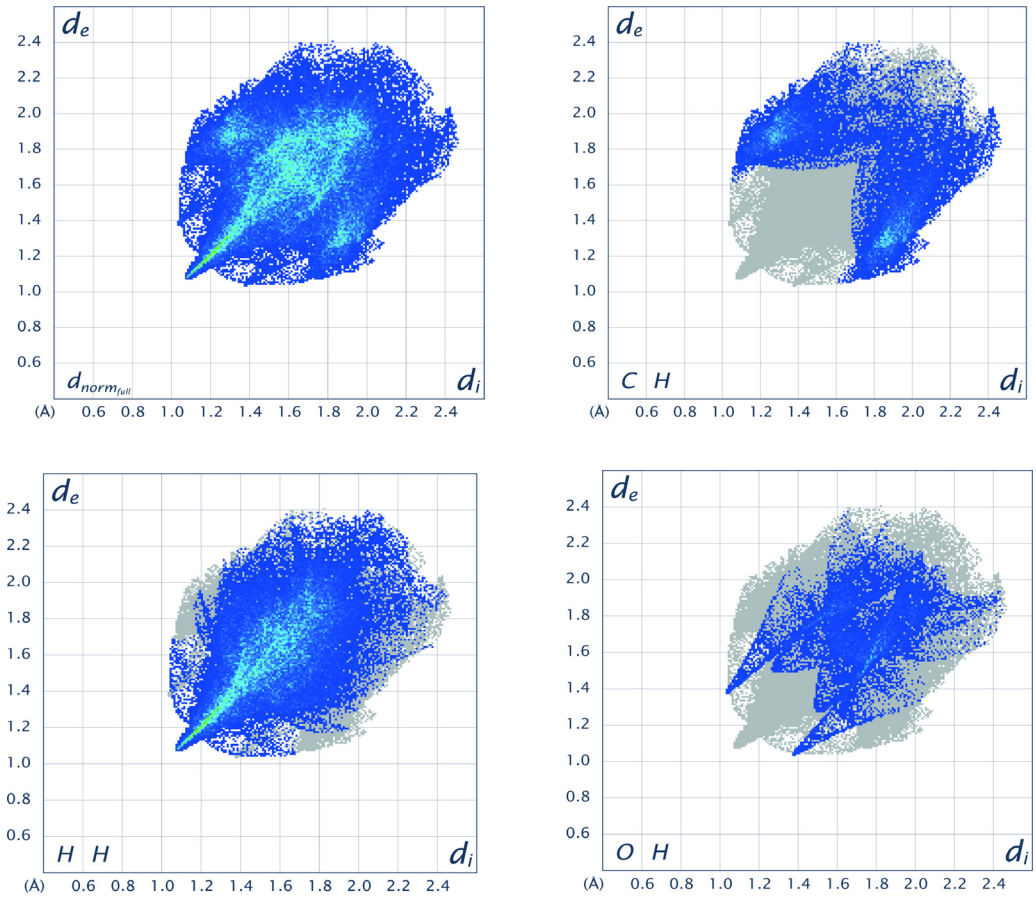

Fig. 4. The full 2D fingerprint plots for the title compound, showing (a) All interactions and those delineated into (b) C…H/H…C (c) H…H (d) O…H/H…O interactions.

Table 2
Reorganization energies and charge transfer rates.

	Reorganization Energy (eV)		Charge Transfer Rates (s^{-1})	
	e^-	h^+	e^-	h^+
C-NMe2	0.37	0.12	1.07×10^{13}	1.73×10^{14}
Pentacene	0.12	0.08	2.59×10^{14}	4.653×10^{14}

transfer rates, k_{CT}, according to the following equation [50,51]

$$k_{CT} = \frac{4\pi^2}{h} \cdot \frac{1}{\sqrt{4\pi\lambda k_B T}} t^2 \exp\left(\frac{-\lambda}{4k_B T}\right)$$

Where, the symbols have their usual meaning. Mathematical analysis of the above equation is straightforward, and it is clear that higher charge transfer rates are obtained if the reorganization energies are low. To assess the charge transfer potential of some molecules, it is the best choice to compare it with the Pentacene molecule, which is one of the important molecules in organic electronics. Table 2 presents the reorganization energies and charge transfer rates for **C–NMe$_2$** and Pentacene molecules. We have adopted the values of reorganization energies and charge transfer rates of Pentacene from papers [52–54].

The Pentacene molecule is characterized by the very low reorganization energies for both electrons and holes, 0.12 eV and 0.08 eV, respectively. The electron reorganization energy of **C–NMe$_2$** is much higher than that of Pentacene. However, the hole reorganization energy is highly competitive. Namely, the hole reorganization energy of **C–NMe$_2$** is 0.12 eV and is just 0.04 eV higher than that of Pentacene. This indicates that the charge transfer rates of holes in the case of the **C–NMe$_2$** molecule could be comparable to that of Pentacene. Indeed, the calculation of charge transfer rates for **C–NMe$_2$** resulted in a lower value than that of Pentacene, but it has the same order of magnitude, which is a promising result. We are also reporting the orientations of dimers with the highest charge transfer rates of electrons and holes, with corresponding intermolecular noncovalent interactions, Figure S2(a) and Figure S2(b). Namely, the dimer for which the highest electron reorganization energy was obtained is characterized by the four noncovalent interactions between **C–NMe2** molecules, while the dimer for which the highest hole reorganization energy obtained is characterized by only two noncovalent interactions which involve oxygen atom of one molecule and hydrogen atoms of benzene ring and methyl groups of another **C–NMe2** molecule.

3.5. Reactivity properties

3.5.1. Frontier molecular orbital analysis

Predicting the electrophilic and nucleophilic sites in organic molecules is a power model for analyzing chemical reactivity of organic species, which helps in better understanding of many organic reactions. Molecular orbitals such as Highest occupied molecular orbital (HOMO) and Lowest unoccupied molecular orbital (LUMO) are the important molecular orbitals which have been used in Frontier Orbital Molecular Theory (FMO). According to FMO theory, the molecular regions where the LUMO is localized, is the electrophilic site due to the presence of highly reactive electrons in this orbital [55,56]. For the title molecule, the energies of the HOMO and LUMO were predicted at B3LYP/6–311 G (d, p) level of theory the electron density distribution of frontier molecular

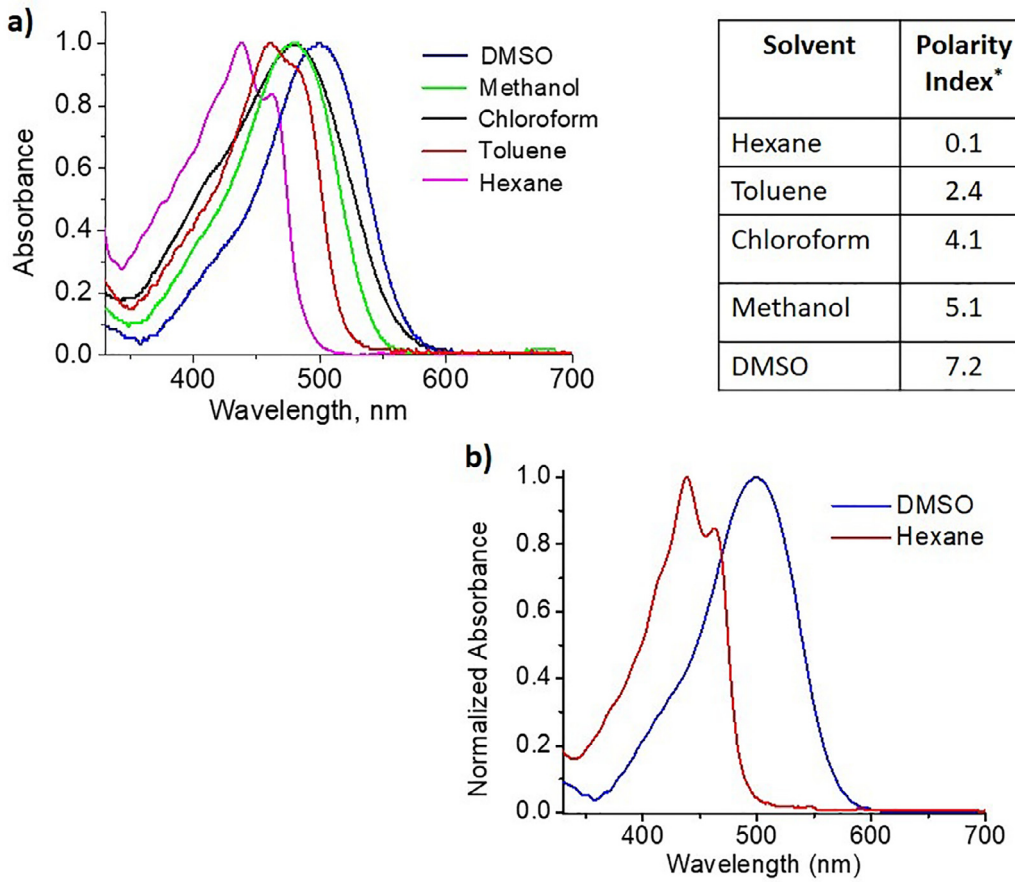

Solvent	Polarity Index*	λ_{max} (nm)
Hexane	0.1	438
Toluene	2.4	460
Chloroform	4.1	480
Methanol	5.1	483
DMSO	7.2	500

Fig. 5. a) Normalized absorption spectrum of C–NMe2 (10 μM) in different polar and non-polar solvents. b) Absorption spectra of C–NMe2 in Hexane (Red) and DMSO (Blue).

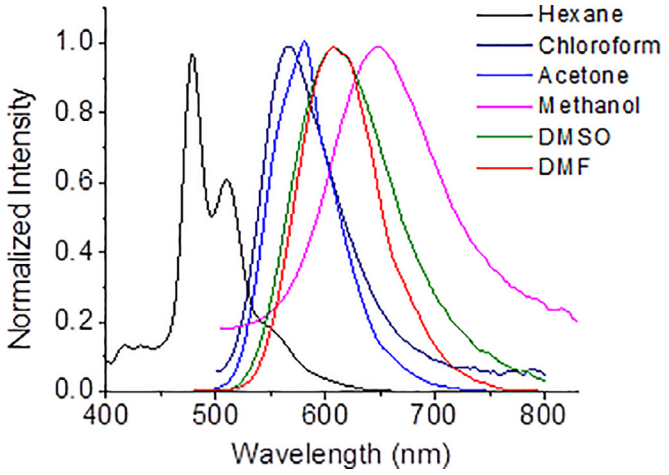

Fig. 6. Normalized fluorescence spectrum of C–NMe2 (10 μM) in different polar and non-polar solvents.

orbitals are presented in Fig. 8. From the electron density distribution profile of frontier molecular orbitals (Fig. 8), it is evident that major part of the HOMO contribution is coming from the two tail ends of the molecule, mainly from the phenyl and methyl carbon atoms. LUMO is concentrated over the central part of the molecule, that is over the carbon bridge and the oxygen atoms of the carbonyl groups, and this indicates that central part of the molecule is highly prone to electrophilic attack. Analysis of frontier molecular orbitals reveals that the central part of the molecule is more likely the preferential sites for the electrophilic attack. The relatively low values of the HOMO-LUMO gap (1.88 eV) and dipole moment (5.963 Debye) indicate low stability of the title compound.

3.5.2. Molecular electrostatic potential (MEP)

Identification of reactive sites in organic molecules helps us to understand the reactive mechanism of chemical reactions. One of the quantum-molecular descriptors which was widely used to identify electrophilic and nucleophilic sites in organic molecules, is MEP descriptor [57]. Since it is very useful for analyzing pi electrons and lone pairs in a molecule, ESP analysis is widely performed on molecular van der Waals (vdW) surfaces. From the analysis of MEP surface (Fig. 9), it is found that the site which is prone to nucleophilic attack is the vicinity of the methyl groups symmetrically attached to the nitrogen atoms on either side of the molecule, which is understood from the red color over the methyl groups. The most reactive part of the molecule, which is sensitive towards the electrophilic attack is the region around two oxygen atoms in the molecule, which is confirmed by the blue color of the MEP surface around two carbonyl groups. The above findings of most reactive sites in the molecule were verified by quantitative analysis of electrostatic potential [58,59] using Multiwfn software [60,61]. Two significant global minima of ESP (−43.77 kcal/mol and −43.21 kcal/mol) are found over the two oxygen atoms, which indicate that the two oxygen atoms of the carbonyl groups are the most favorable sites for electrophilic attack. The positive values for ESP (+25.26 kcal/mol and +25.66 kcal/mol) are much

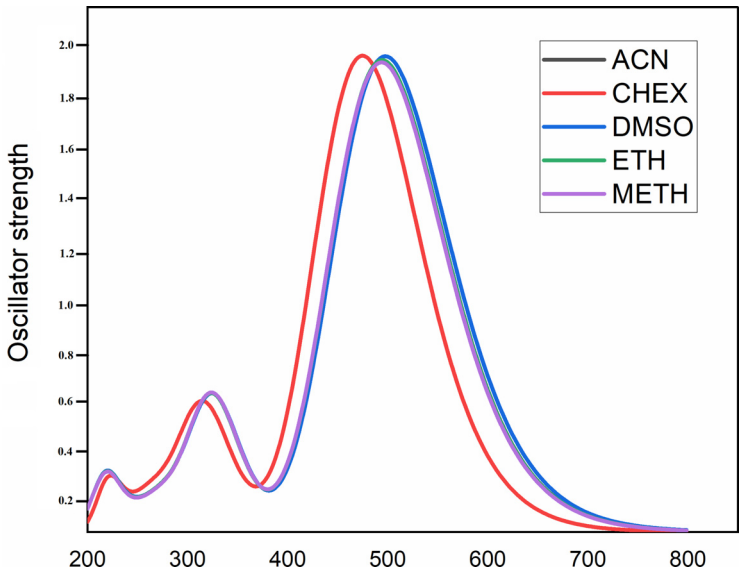

Fig. 7. UV/Vis absorption spectra of the title compound calculated at IEF-PCM: B3LYP/6–311 G (d, p) level of theory in (a) Acetonitrile (black) (b) Cyclohexane (red) (c) DMSO (blue) (d) Ethanol (green) and Methanol (violet).

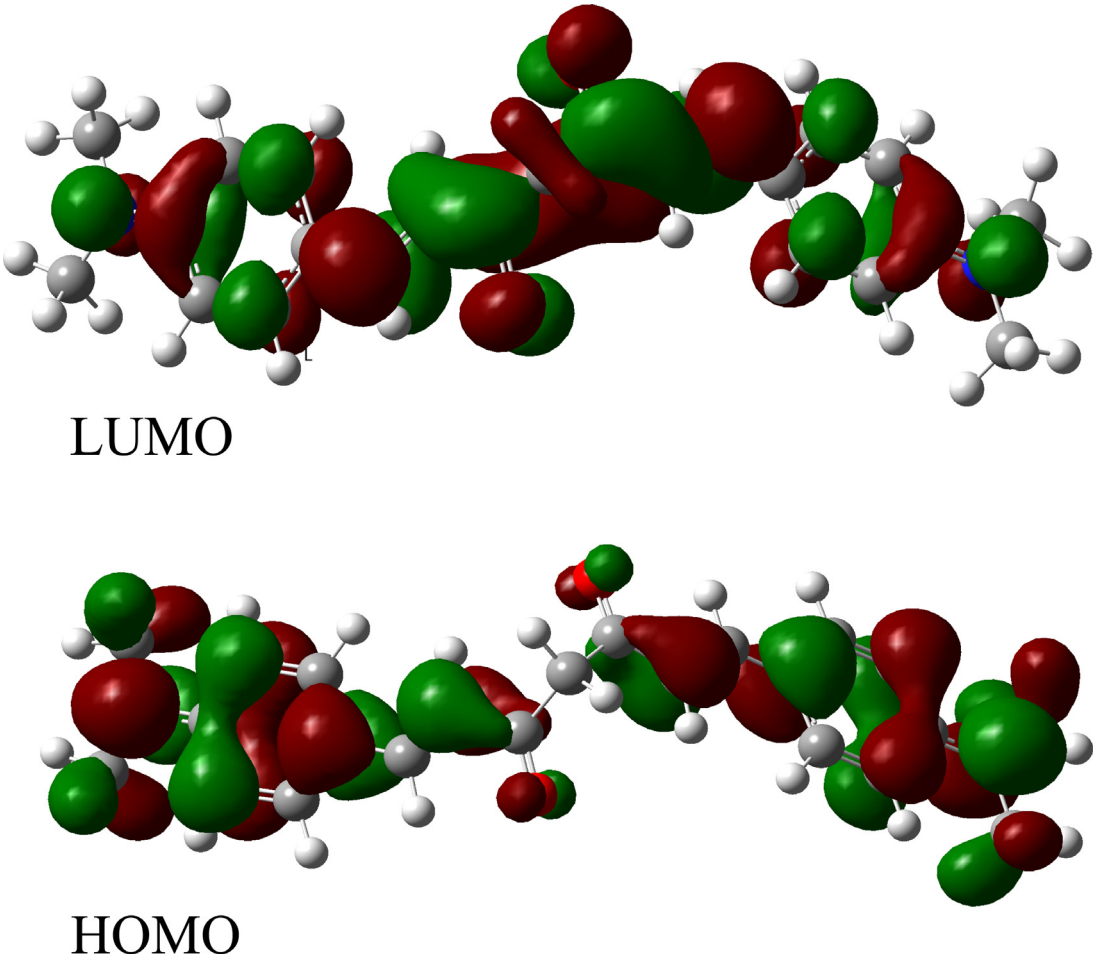

Fig. 8. Contour plots of the HOMO and LUMO for the title compound.

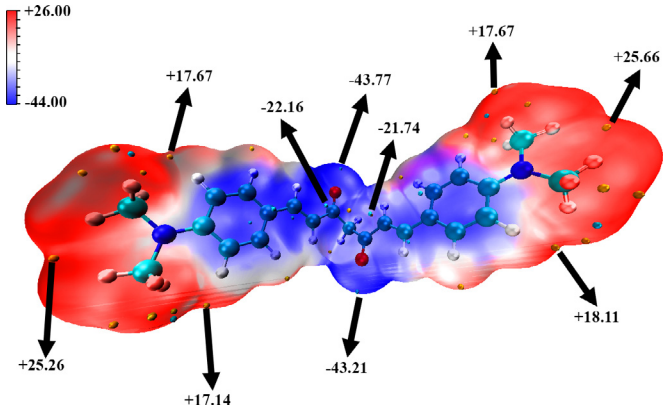

Fig. 9. MEP surface of the title compound along with Electrostatic potential values.

larger around the methyl groups and this high value of ESP may be attributed to the presence of nitrogen atoms attached to the two phenyl rings, which attracts electrons from methyl carbon atoms.

3.6. Evaluation of biological activity

3.6.1. Protein-Ligand interactions

The crystal structures of the two proteins, PLpro (PDB ID - 7JRN) [62] and ADRP (PDB ID - 6WO2) [63] were downloaded from protein data bank (PDB). AutoDock 4.2 software [64] was used to perform all molecular docking calculations The crystal structures of the two proteins, PLpro (PDB ID - 7JRN) [62] (SARS-CoV-2 papain-like protease) and ADRP (PDB ID - 6WO2) [63] (SARS-CoV-2 ADP ribose phosphatase) were downloaded from protein data bank (PDB). The default protonation of ionizable residues in the proteins were set at pH 7.4 and polar hydrogens were added to the crystal structures of the proteins, prior to the docking process. The docking protocol was tested by removing co-crystallized ligands from the protein crystal structures and docking in the same binding sites. The root mean square deviation (RMSD) between the co-crystallized ligands and their re-docked confirmations were calculated for each crystal structure and found to be equal to less than 1 Å. After validating the docking protocol, we carried out docking studies to explore the binding modes of the title compound with the PLpro and ADRP enzymes. The active sites in the protein crystal structures were found out by determining the centroid coordinates of each protein and co-crystallized ligands using Discover Studio Visualizer 4.0 [65] and is used as the active sites for the docking studies.

The dimensions of the active site coordinates used were $x = 17.873$ Å, $y = 63.929$ Å, $z = -5.142$ Å and grid box with radius of $40 \times 40 \times 40$ Å^3 was generated, for 7JRN and for 6W02, the dimensions of the active site coordinates used were $x = -0.151$ Å, $y = -7.437$ Å, $z = -21.716$ Å and grid box with radius of $50 \times 50 \times 50$ Å^3 was generated. Lamarckian Genetic algorithm available in AutoDock was used to model the interaction modes between the receptors and the title molecule. Initial position, orientation, and torsions of the ligand molecules were set erratically. Each docking simulation was derived from 50 different runs that were set to cease after a maximum of 2,500,000 energy evaluations. The population size was set to 300 and during the search, a translational step of 0.2 Å, quaternion and torsion steps of 5 were applied. In the case of each protein structures, out of fifty docked confirmations obtained, one which has lowest binding energy were selected (−8.81 kcal/mol for 6W02 and −7.71 kcal/mol for 7JRN) and analysed for detailed interactions of title molecule with the amino acid residues.

Post-docking analysis of protein-ligand complex revealed that the title compound is inserted well in to the binding pocket of the ADRP protein and PLpro proteins and occupy their respective active sites Figs. 10a and 10b. From the obtained 2D interaction diagrams of ligand-protein complex (Fig. 11a), it is clear that the title compound forms a strong hydrogen bond (2.09 Å) with the PLpro protein between one of the carbonyl oxygen bonds and the hydroxyl group of Threonine residue (Thr301). The other significant interactions of the title compound with the PLpro protein residues such as Pro248, Tyr268, Asp164, Gly163 and Leu162 are hydrophobic in nature. The 2D interaction diagram (Fig. 11b) revealed that compound forms a strong hydrogen bond (1.77 Å) with the ADRP protein between one of the carbonyl oxygen bonds and the amino group of Leucine residue (Leu126). In addition to this, the compound exhibits two hydrophobic interactions with amino acid residues Val49, Ala38, Phe132, Ile131, Ala52, Asp22 and Phe156.

3.6.2. Stability of ligand-protein complexes using md simulations

MD simulations serve as an important supporting tool that validates results of molecular docking studies [66]. The analyses of MD simulations help to examine the stability as well as the dynamic behavior of the docked protein-ligand complex [67]. In MD simulations, the conformational stability and dynamic behavior of the protein-ligand complexes were investigated at 100 ns simulation period. Trajectory analyses of Root Mean Square Deviation (RMSD), Root Mean Square Fluctuation (RMSF), Radius of gyration (Rg), and

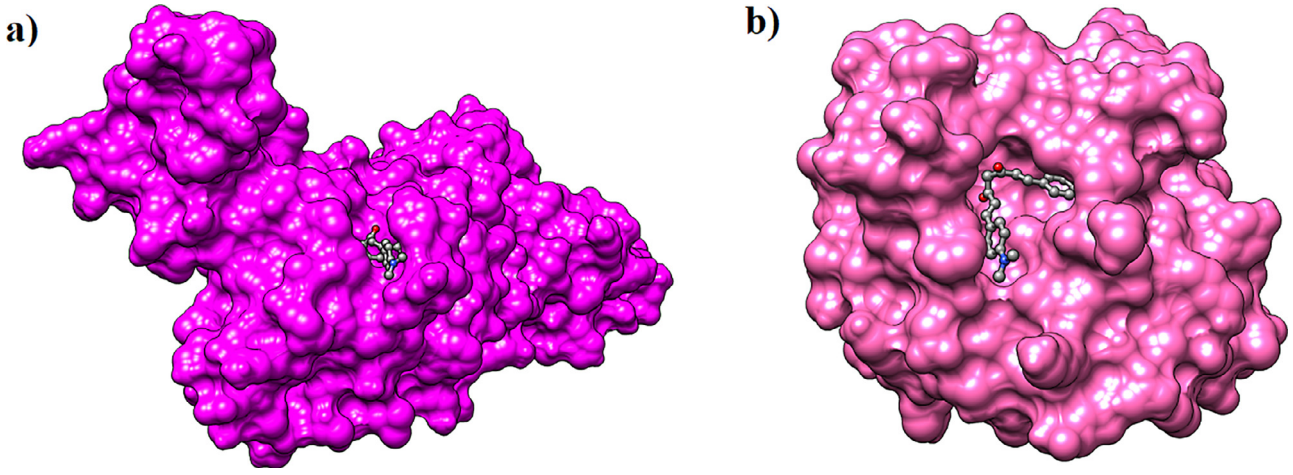

Fig. 10. 3D surface representation of the binding poses of the title compound at the binding site of (a) ADRP protein (b) PLpro protein.

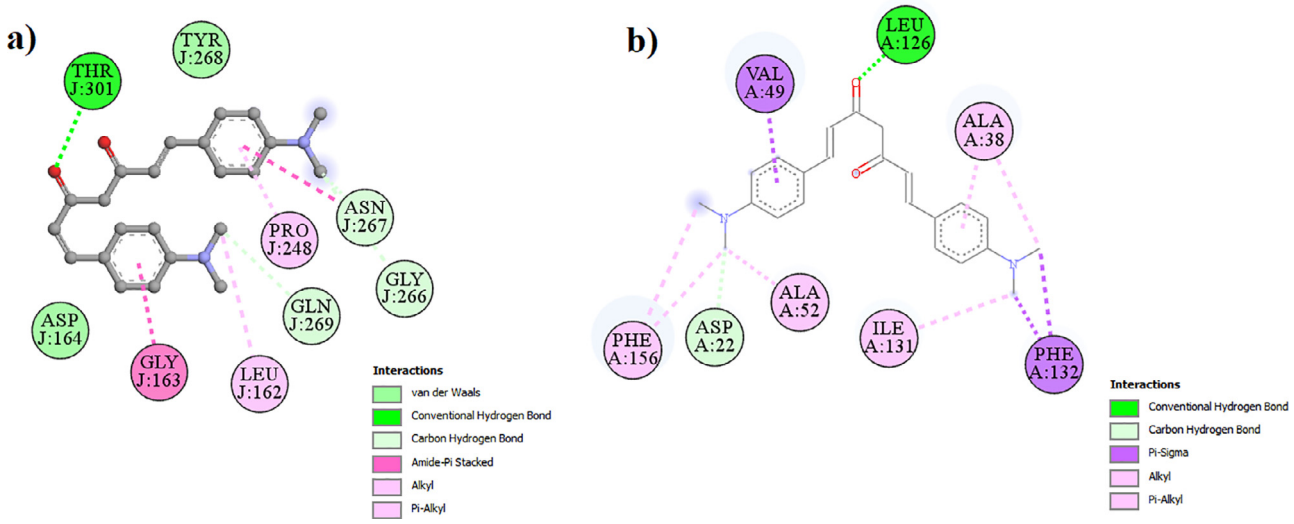

Fig. 11. 2D representation of Protein-Ligand interactions for (a) PLpro- C–NMe2 complex (b) ADRP- C–NMe2 complex.

intermolecular H bonds numbers were recorded. RMSD measurement is the most important parameter used to measure the stability of the protein-ligand [68]. A RMSD value of less than 0.3 nm indicates that the system is highly stable and lower this value is, higher the protein stability [69]. RMSF, a measure of protein fluctuation, is another important parameter that indicates the stability of bound protein-ligand complexes [70]. The smaller value of Rg and its stability during the simulation period is an indicator of the stability of both the protein and protein-ligand complex [71]. The formation of hydrogen bonds in protein-ligand interactions drives the ligand to have more affinity for the receptor molecule [41]. A ligand that forms as many hydrogen bonds as possible with the active site residues of the target protein molecule is said to produce a well-defined and strong protein-ligand interaction [43]. In MD simulations, measuring the number of hydrogen bonds formed by the ligand with a protein molecule is also an important property for the determination of the strength and stability of the protein-ligand complex [72]. The graphs of *RMSD, RMSF, Rg* and H bonds numbers of **PLpro- C–NMe2** and **PLpro-TTT** complexes are presented in Fig. 12.

The RMSD trajectory of the **PLpro- C–NMe2** complex showed fluctuations over the range between 0.2 nm and 0.3 nm with the majority of fluctuations were occurred between 0.25 nm and 0.35 nm from 20 ns to 80 ns. The fluctuations ended up at 0.4 nm and the system became stable for rest of the simulation period. Similar *RMSD* trajectory was observed for the **PLpro-TTT** complex but to a considerably lesser extent (Fig. 12a). Such *RMSD* trajectory clearly suggests the formation of a stable ligand conformation for **C–NMe$_2$** on the active binding site(s) of PLpro at the end of simulation period. The fluctuation data of each amino acid for **PLpro-C–NMe2** and **PLpro-TTT** complexes were recorded. As the simulation proceeds, reduced fluctuations of the system were observed. Maximum fluctuations were seen between 0.2 ns and 0.4 ns. This suggests that ligand binding reduces fluctuations at the binding site, but increases fluctuations at other sites. It is also evidence of stronger interaction of the **C–NMe2** with **PLpro**. The fluctuation data of **PLpro- C–NMe2** were to some extent similar to **PLpro-TTT** (Fig. 12b). As the homogeneity of *RMSF* was maintained for the studied complexes throughout the simulation period, the *RMSF* data supports and substantiates the RMSD trajectory of the studied protein-ligand complexes. The *Rg* trajectories of **PLpro- C–NMe2** and **PLpro-TTT** complexes fluctuate between 2.35 nm and 2.45 nm for up to 90 ns and stabilized at 2.50 nm for the rest of the simulation period (Fig. 12c). Analysis of *Rg* trajectories reveals that **C–NMe2** produced better interaction with **PLpro** through the formation of a stable complex over the simulation period. Further, results of H bonds numbers reveal that a good numbers of hydrogen bonds were formed between **PLpro** and **C–NMe2** throughout the 100 ns simulation (Fig. 12d).

Further investigation of hydrogen bonding during the MD simulation period was carried out by analyzing protein-ligand interactions in terms of H bond formation. Fig. 13 shows 3D binding poses and 2D interaction diagrams of change of H bond formation between **C–NMe2** and **PLpro** at the middle (50 ns) and the end (100 ns) of simulation period. During the 50 ns simulation, **C–NMe2** formed only one H bond with the Gln268 residue, whereas **C–NMe2** formed two H bonds with Tyr112 and Val165 residues in 100 ns simulation. This study proves that **C–NMe2** forms more stable and stronger complex with the **PLpro** during 100 ns simulation.

The RMSD trajectory of the **ADRP- C–NMe2** complex exhibited fluctuations over the range between 0.1 nm and 0.25 nm with the majority of fluctuations were occurred between 0.15 nm and 0.20 nm from 20 ns to 80 ns. The fluctuations ended up at 0.3 nm and the protein-ligand complex became stable between 90 ns and 100 ns. In case of **ADRP-APR (cocrystal adenosine-5-diphosphoribose)** complex, similar *RMSD* trajectory was observed (Fig. 14a). From *RMSD* trajectories, it is apparent that a stable ligand conformation was generated on the active binding site(s) of **ADRP** at around 90-95 ns. In RMSF trajectory analysis, the fluctuation data for **ADRP- C–NMe2** and **ADRP-APR** complexes were obtained. As the simulation proceeds, reduced fluctuations of the system were observed. Maximum fluctuations were seen between 0.2 ns and 0.4 ns. This clearly reflects that ligand binding reduces fluctuations at the active binding site and increases at remote sites. This indicates a stronger interaction of **C–NMe2** with **ADRP**. The fluctuation data of **ADRP- C–NMe2** were more or less similar to **ADRP-APR** (Fig. 14b). As the homogeneity of *RMSF* was maintained throughout the simulation period, the *RMSF* data concords and substantiates the *RMSD* trajectory of the studied protein-ligand complexes. The *Rg* trajectories of **ADRP- C–NMe2** and **ADRP-APR** complexes fluctuate between 1.52 nm and 1.55 nm for up to 80 ns and stabilized at 1.54 nm at the end of the simulation period (Fig. 14c). Analysis of *Rg* trajectories shows that **C–NMe$_2$** shows good interaction with **ADRP** with the formation of a stable complex over the simulation period. Results of H bonds numbers

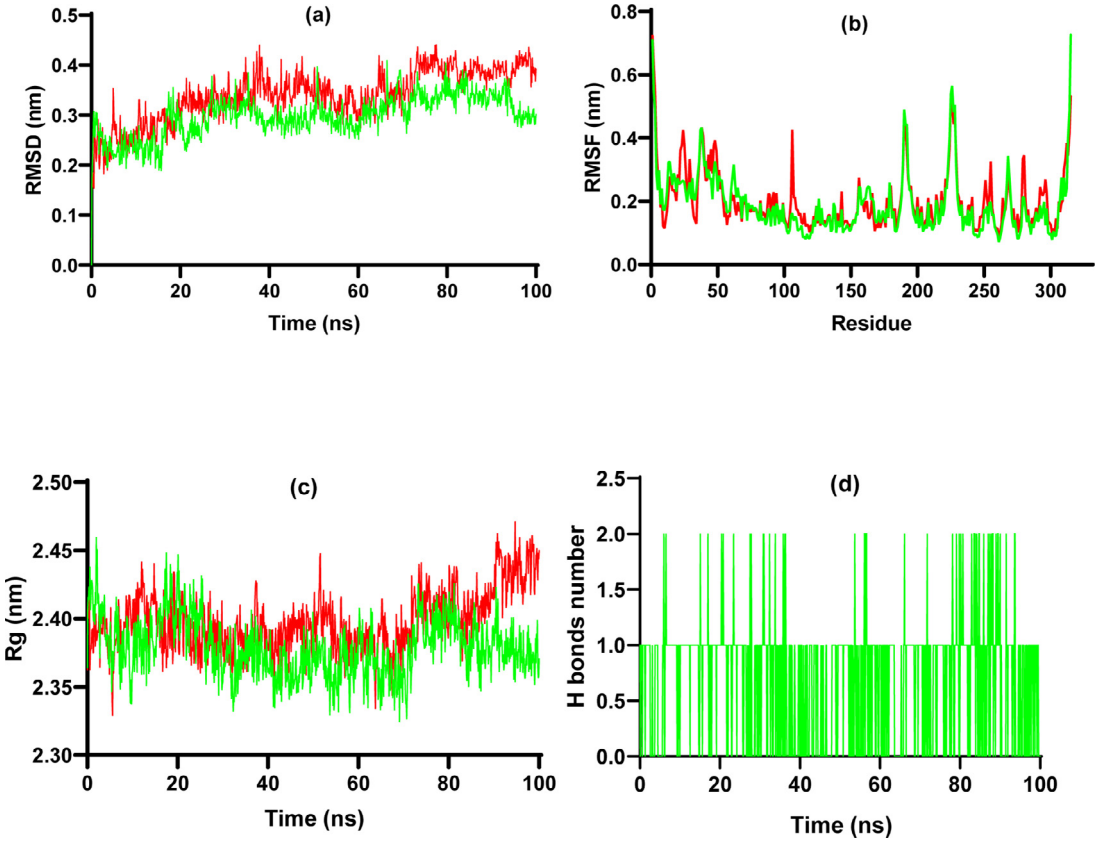

Fig. 12. Trajectory analysis of molecular dynamics simulation of SARS-CoV-2 papain-like protease (PLpro) with C–NMe2 (PLpro- C–NMe2), and cocrystal GRL0617 (PLpro-TTT) (a) Root mean square deviation (RMSD) of compound PLpro-CUR, and PLpro-CUR complexes (b) Root mean square fluctuation (RMSF) (c) Radius of gyration (Rg) values, and (d) Hydrogen bonds number between PLpro and CUR throughout the 100 ns simulation. (PDB ID: 7JRN).

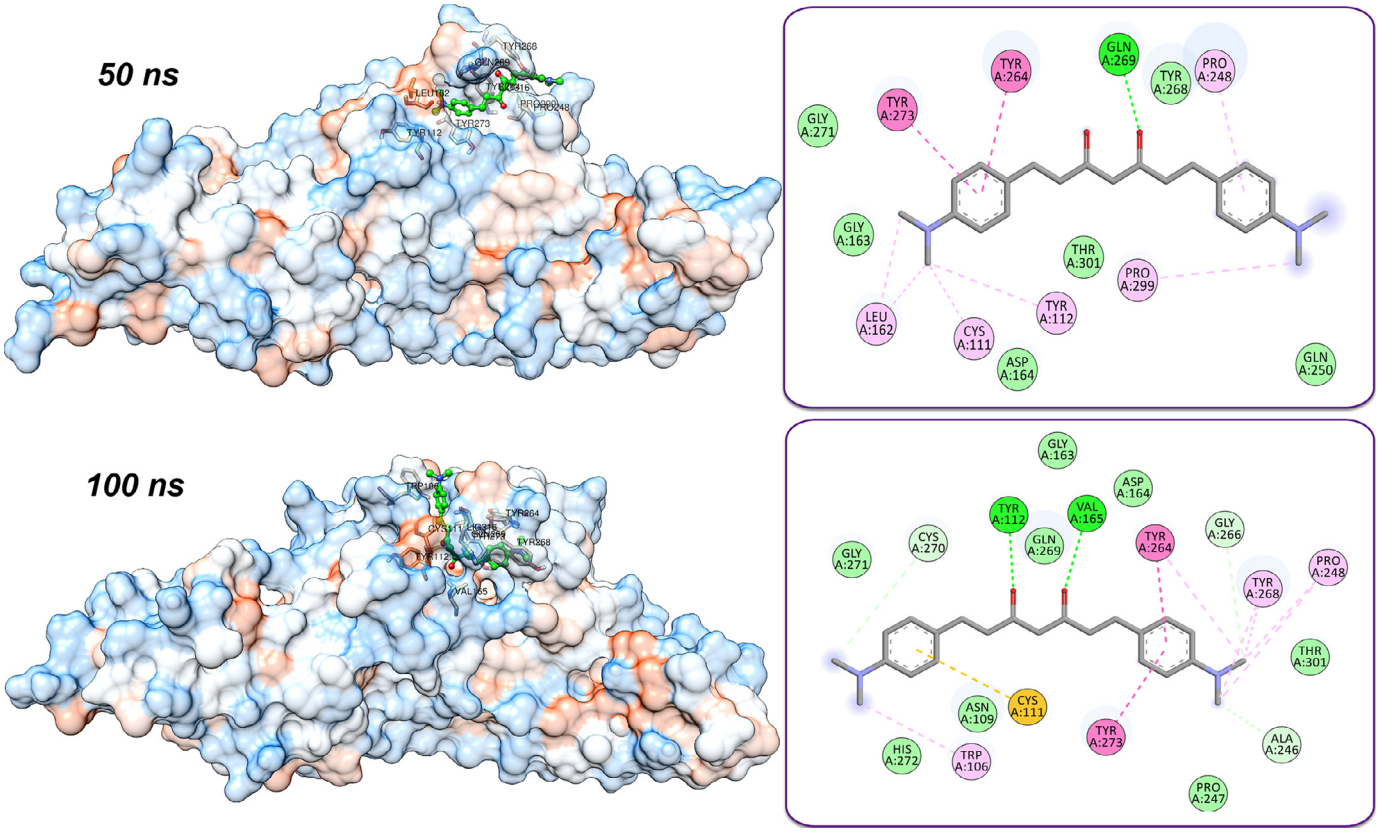

Fig. 13. Binding pose (left) and schematic interactions diagram (right) of change at the SARS-CoV-2 papain-like protease (PLpro) active site with C–NMe2 at the middle, and end of the 100 ns molecular dynamics simulations.

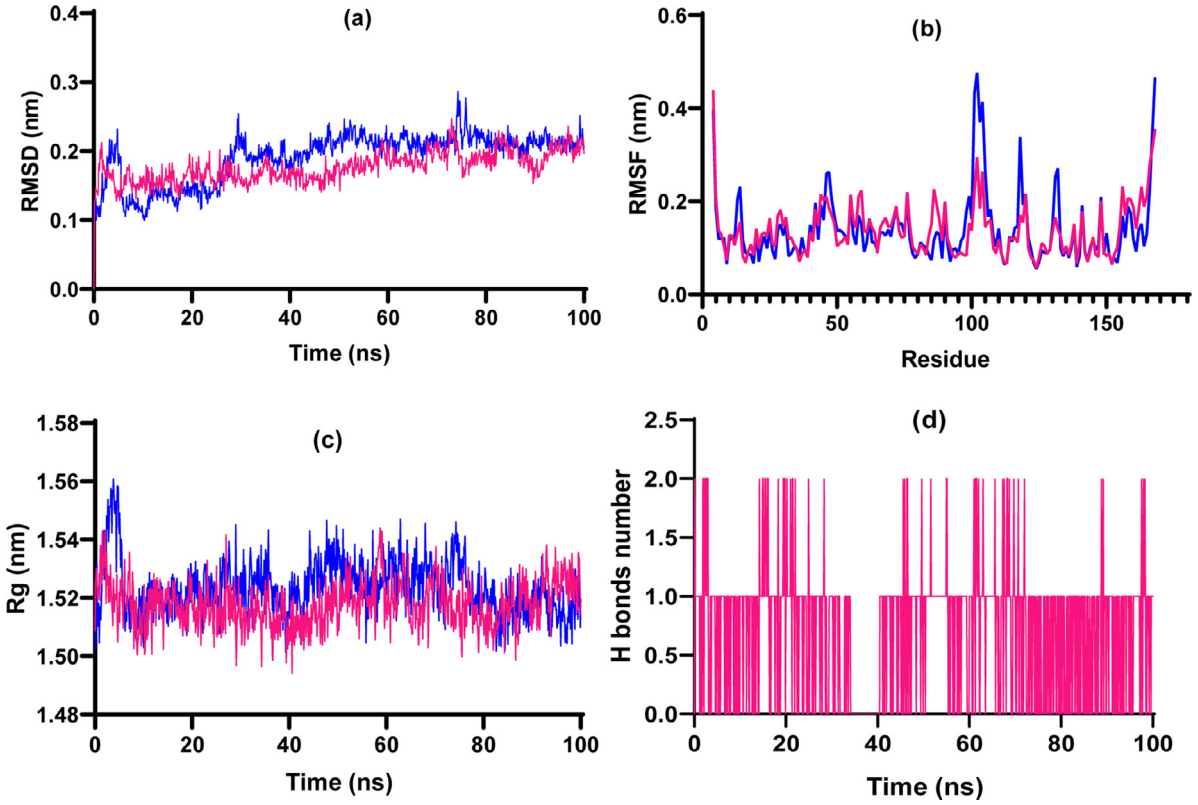

Fig. 14. Trajectory analysis of Molecular dynamics simulation of C–NMe2 and cocrystal adenosine-5-diphosphoribose (APR) with SARS-CoV-2 ADP ribose phosphatase (ADRP). (a) RMSD of ADRP- C–NMe2 and ADRP-APR complexes, (b) RMS fluctuation, (c) Rg values, (d) and hydrogen bonds number between ADRP and C–NMe2 during the 100 ns period of simulation (PDB ID: 6W02).

Table 3
Results of MM-PBSA interaction-free binding energies calculation between SARS-CoV-2 papain-like protease (PLpro) and curcumin derivative (CUR) and cocrystal ligand GRL0617 (TTT), and free binding energies between SARS-CoV-2 ADP ribose phosphatase (ADRP) and CUR and cocrystal adenosine-5-diphosphoribose (APR).

	enzyme-ligand complexes			
	papain-like protease		ADP ribose phosphatase	
Parameters (Energy)	PLpro- C–NMe2 (kJ/mol)	PLpro-TTT (kJ/mol)	ADRP-C-NMe2 (kJ/mol)	ADRP-APR (kJ/mol)
Van der Waals	−213.329 ± 23.724	−176.438 ± 12.160	−145.392 ± 11.280	−267.340 ± 12.294
Electrostatic	−10.658 ± 5.895	−17.351 ± 5.246	−12.118 ± 4.033	−7.185 ± 4.774
Polar solvation	90.803 ± 18.722	75.658 ± 9.256	43.933 ± 6.261	117.554 ± 9.499
SASA	−20.187 ± 1.735	−17.084 ± 1.047	−13.382 ± 1.161	−23.132 ± 0.926
Binding free	**−153.371 ± 16.514**	**−135.215 ± 11.877**	**−126.958 ± 11.580**	**−180.103 ± 11.717**

SARS-CoV-2 PLpro: SARS-CoV-2 papain-like protease; **C–NMe2**: Title compound; **TTT**: SARS-CoV-2 PLpro cocrystal ligand GRL0617; **ADRP**: SARS-CoV-2 ADP ribose phosphatase; **ARP**: SARS-CoV-2 ADRP cocrystal ligand adenosine-5-diphosphoribose.

indicates that a good numbers of hydrogen bonds were formed between **ADRP** and **C–NMe2** throughout the 100 ns simulation (Fig. 14d).

Further investigation of hydrogen bonding during the MD simulation was carried out by analyzing protein-ligand interactions in terms of H bond formation. Fig. 15 shows 3D binding poses and 2D interaction diagrams of change of H bond formation between **C–NMe2** and **ADRP** at the middle (50 ns) and the end (100 ns) of simulation period. During the 50 ns simulation, **C–NMe2** formed only one H bond with the Leu126 residue, whereas **C–NMe2** formed two H bonds with Leu126 and Gly130 residues in 100 ns simulation. This study proves that **C–NMe2** forms more stable and stronger complex with the **ADRP** during 100 ns simulation.

3.6.3. MM-PBSA analysis

The MM-PBSA binding free energy represents the amount of energy generated as a result of protein-ligand interaction [73]. The binding free energy is a cumulative sum of Van der Waals, electrostatic, polar solvation and *SASA* energies. A low binding free energy is an indication of the formation of a more stable protein-ligand complex [74]. Results of MM-PBSA binding free energies of the protein-ligand complexes studied for MD simulations are given in Table 3. In the case of **SARS-CoV-2 PLpro**, a lower binding free energy was obtained for the **PLpro- C–NMe$_2$** complex (−153.371 ± 16.514 kJ/mol) as compared to the **PLpro-TTT** (−135.215 ± 11.877 kJ/mol). It suggests that the compound **C–NMe$_2$** formed more stable complex than the cocrystal ligand **TTT** with the **PLpro** protein. For **SARS-CoV-2 ADRP**, the binding free energy of the **ADRP- C–NMe$_2$** complex (−126.958 ± 11.580 kJ/mol) was found comparatively higher than that of **ADRP-APR** complex (−180.103 ± 11.717 kJ/mol). It reveals that the interaction of the compound **C–NMe$_2$** with the **ADRP** protein was less stable than that with the cocrystal ligand **APR**. From binding free energy calculations, it can be inferred that the compound **C–NMe$_2$** exhibited

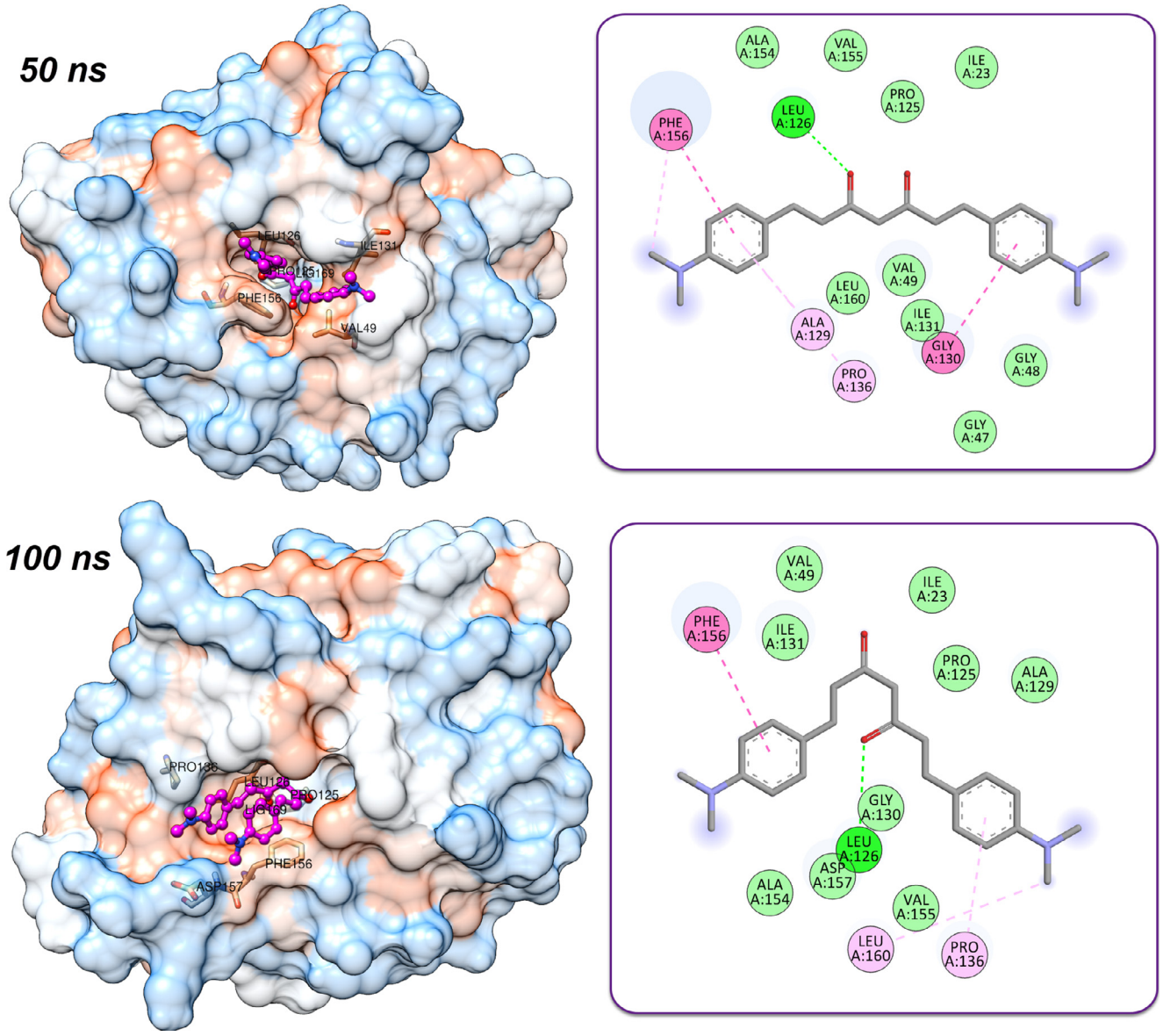

Fig. 15. Binding pose (left) and schematic interactions diagram (right) of change at the SARS-CoV-2 ADP ribose phosphatase (ADRP) active site C–NMe2 at the middle, and end of the 100 ns molecular dynamics simulations.

better interaction with the formation of a more stable complex with the **SARS-CoV-2 PLpro** over **SARS-CoV-2 ADRP**.

4. Conclusions

In conclusion, we have successfully synthesized a dimethylamino derivative of Curcumin and molecular structure was characterised by spectroscopic techniques and single crystal X-ray diffraction. The title compound crystallizes in the monoclinic space group P21/n. From the detailed analysis of crystal structure using Hirshfeld surface, it is found that the hydrogen bond and van der Waals interactions play the major roles in the crystal packing. The absorption spectrum of C–NMe2 in various solvents exhibit the significant changes in the absorption spectra with marginal shift in the absorption maxima of C–NMe2 in polar and non-polar solvents. The dimethylamino derivative showed considerable red shift in emission spectrum when compared to its parent compound Curcumin in most of the organic solvents. These provided valuable insight into the photophysical properties which suggest that the dimethylamino curcuminoid (**C–NMe2**) may be used for various sensing and imaging applications. Reactivity properties and optoelectronic properties were studied using DFT and MD calculations. The MD calculations revealed the high stability of the title compound and suggested that it is reasonable to consider polyvinylpyrrolidone polymer as an excipient for title molecule. Molecular docking studies revealed that the title compound has better activity against two replicative proteins (SARS-CoV-2 PLpro and SARS-CoV-2 ADRP) of COVID-19 virus and stability of the protein-ligand complexes were studies using MD simulations and MM-PBSA analysis. **C–NMe2** exhibited better interaction with SARS-CoV-2 PLpro over SARS-CoV-2 ADRP. The stability of the complex is attained through hydrogen bonds and hydrophobic interactions. Here the in-silico investigations about the structural characteristics and interaction of **C–NMe2** with viral proteins unveiling the potential of a Curcumin analogue with better optoelectronic properties for clinical applications. Photodynamic therapy application of the boron containing **C–NMe2** also in our future plan.

Author contribution statement

VKA and **KVDB**: conceived the idea, planned and performed the experimental work, analyzed absorption and emission spectra, discussed the results and cooperated in the preparation of the manuscript. **ISD** analyzed the crystal structure. **SJA and SA** performed MD simulations for analyzing the stability and optoelectronic properties and cooperated in interpreting the results. **JBB**: Cooperated in the preparation of the manuscript and interpretation of the results. **IC** and **MR** carried out Molecular Dynamics and MM-PBSA studies and interpreted the results. **RR**: Planned, designed ab initio calculations, analyzed results, compiled and draft the manuscript with input from all coauthors.

Declaration of Competing Interest

All authors have participated in (a) conception and design, or analysis and interpretation of the data; (b) drafting the article or revising it critically for important intellectual content; and (c) approval of the final version. This manuscript has not been submitted to, nor is under review at, another journal or other publishing venue.

Data availability

Data will be made available on request.

Acknowledgement

The authors VPA and KVD acknowledge the support of Analytical Discipline and Centralized Instrument Facility Central Salt and Marine Chemicals Research Institute, Bhavnagar Gujarat. SJA and SA acknowledge the financial support of the Ministry of Education, Science and Technological Development of the Republic of Serbia (Grant No. 451–03–9/2021–14/200125). Special thanks to WEBGRO Macromolecular Simulations (https://simlab.uams.edu/index.php) providing high performance computing for their MD simulations. RR would like to acknowledge Dr. B. Harikumar, Former Head, Department of Chemistry, T.K.M. College of Arts and Science, Kollam, Kerala, India for providing Computational facility for doing DFT calculations using Gaussian 09 software.

Supplementary materials

Figure S1. Figure S1. a) and b) are the emission spectra of C–NMe2 in ethanol at 77 K and 298 K. c) and d) are the emission spectra of C–NMe2 in hexane at 77 K and 298 K.

Supplementary material associated with this article can be found, in the online version, at doi:10.1016/j.molstruc.2023.135110.

References

[1] C. Ceraolo, F.M. Giorgi, Genomic variance of the 2019-nCoV coronavirus, Journal of Medical Virology 92 (2020) 522–528, doi:10.1002/jmv.25700.
[2] S. Farhadian, E.H. Soureshjani, F.H. Shahraki, A.H. Dehkordi, V.N. Uversky, M. Shirani, B. Shareghi, M. Sadeghi, E. Pirali, S.H. Alijanvand, Identification of SARS-CoV-2 surface therapeutic targets and drugs using molecular modeling methods for inhibition of the virus entry, Journal of Molecular Structure 1256 (2022) 132488, doi:10.1016/j.molstruc.2022.132488.
[3] M.A. Tomeh, R. Hadianamrei, X. Zhao, A Review of Curcumin and its derivatives as anticancer agents, International Journal of Molecular Sciences 20 (2019) 1033, doi:10.3390/ijms20051033.
[4] C.V.B. Martins, D.L. da Silva, A.T.M. Neres, T.F.F. Magalhães, G.A. Watanabe, L.V. Modolo, A.A. Sabino, Â. de Fátima, M.A. de Resende, Curcumin as a promising antifungal of clinical interest, Journal of Antimicrobial Chemotherapy 63 (2008) 337–339, doi:10.1093/jac/dkn488.
[5] S.J. Hewlings, D.S. Kalman, Curcumin: A Review of Its Effects on Human Health, Foods 6 (2017) 10–92, doi:10.3390/foods6100092.
[6] S.Z. Moghadamtousi, H.A. Kadir, P. Hassandarvish, H. Tajik, S. Abubakar, K. Zandi, A Review on Antibacterial, Antiviral, and Antifungal activity of Curcumin, Bio Med Research International 12 (2014) *2014*, doi:10.1155/2014/186864.
[7] Thimmulappa, R. K., Mudnakudu-Nagaraju, K.K., Shivamallu, C., Subramaniam, K. J. T., Radhakrishnan, A., Bhojraj, S., & Kuppusamy, G. (2021). Antiviral and immunomodulatory activity of curcumin: A case for prophylactic therapy for COVID-19. *Heliyon, 7(2),* e06350. https://doi.org/10.1016/j.heliyon.2021.e06350.
[8] K.S. Pawar, R.N. Mastud, S.K. Pawar, S.S. Pawar, R.R. Bhoite, R.R. Bhoite, M.V. Kulkarni, A.R. Deshpande, Oral Curcumin with piperine as adjuvant therapy for the treatment of COVID-19: A randomized clinical Trial, Frontiers in Pharmacology 12 (2021) 1056, doi:10.3389/fphar.2021.669362.
[9] N. Saber-Moghaddam, S. Salari, S. Hejazi, M. Amini, Z. Taherzadeh, S. Eslami, S.M. Rezayat, M.R. Jaafari, S. Elyasi, Oral nano-curcumin formulation -efficacy in management of mild to moderate hospitalized coronavirus disease-19 patients: An open label nonrandomized clinical trial, Phytotherapy research 35 (5) (2021) 2616–2623, doi:10.1002/ptr.7004.
[10] D. Dourado, D.T. Freire, D.T. Pereira, L. Amaral-Machado, É.N. Alencar, A.L.B. de Barros, E.S.T. Egito, Will curcumin nanosystems be the next promising antiviral alternatives in COVID-19 treatment trials? Biomedicine & Pharmacotherapy 139 (2021) 111578, doi:10.1016/j.biopha.2021.111578.
[11] S.M. Khopde, K. Indira Priyadarsini, D.K. Palit, T. Mukherjee, Effect of Solvent on the Excited-state Photophysical Properties of Curcumin, Photochemistry and photobiology 72 (5) (2000) 625–631, doi:10.1562/0031-8655(2000)0720625EOSOTE2.0.CO2.
[12] M. Sharma, U. Pal, M. Kumari, D. Bagchi, S. Rani, D. Mukherjee, A. Bera, S.K. Pal, T. Saha Dasgupta, S. Mozumdar, Effect of solvent on the photophysical properties of isoxazole derivative of curcumin: a combined spectroscopic and theoretical study, Journal of Photochemistry and Photobiology A: Chemistry 410 (2021) 113164, doi:10.1016/j.jphotochem.2021.113164.
[13] S. Mondal, S. Ghosh, S.P. Moulik, Stability of curcumin in different solvent and solution media: UV–visible and steady-state fluorescence spectral study, Journal of Photochemistry and Photobiology B: Biology 158 (2016) 212–218, doi:10.1016/j.jphotobiol.2016.03.004.
[14] M. Dei Cas, R. Ghidoni, Dietary curcumin: correlation between bioavailability and health potential, Nutrients 11 (9) (2019) 2147, doi:10.3390/nu11092147.
[15] M. Sharma, S. Rani, S. Mozumdar, Perturbations in the photophysical properties of isoxazole derivative of curcumin up on interaction with different anionic, cationic and non-ionic surfactants, Journal of Molecular Liquids 343 (2021) 116981, doi:10.1016/j.molliq.2021.116981.
[16] A. Sreedhar, I. Sarkar, P. Rajan, J. Pai, S. Malagi, V. Kamath, R. Barmappa, Comparative evaluation of the efficacy of curcumin gel with and without photo activation as an adjunct to scaling and root planing in the treatment of chronic periodontitis: A split mouth clinical and microbiological study, Journal of Natural Science, Biology, and Medicine 6 (Suppl 1) (2015) S102, doi:10.4103/0976-9668.166100.
[17] E. Asteriou, A. Gkoutzourelas, A. Mavropoulos, C. Katsiari, L.I. Sakkas, D.P. Bogdanos, Curcumin for the management of periodontitis and early ACPA-positive rheumatoid arthritis: killing two birds with one stone, Nutrients 10 (7) (2018) 908, doi:10.3390/nu10070908.
[18] Y. Erez, I. Presiado, R. Gepshtein, D. Huppert, Temperature dependence of the fluorescence properties of curcumin, The Journal of Physical Chemistry A 115 (40) (2011) 10962–10971, doi:10.1021/jp206176p.
[19] L.G. Santin, E.M. Toledo, V.H. Carvalho-Silva, A.J. Camargo, R. Gargano, S.S. Oliveira, Methanol solvation effect on the proton rearrangement of curcumin's enol forms: an ab initio molecular dynamics and electronic structure viewpoint, The Journal of Physical Chemistry C 120 (36) (2016) 19923–19931, doi:10.1021/acs.jpcc.6b02393.
[20] C. Banerjee, S. Ghosh, S. Mandal, J. Kuchlyan, N. Kundu, N. Sarkar, Exploring the photophysics of curcumin in zwitterionic micellar system: An approach to control ESIPT process in the presence of room temperature ionic liquids (RTILs) and anionic surfactant, The Journal of Physical Chemistry B 118 (13) (2014) 3669–3681, doi:10.1021/jp411778q.
[21] Y. Erez, R. Simkovitch, S. Shomer, R. Gepshtein, D. Huppert, Effect of acid on the ultraviolet–visible absorption and emission properties of curcumin, The Journal of Physical Chemistry A 118 (5) (2014) 872–884, doi:10.1021/jp411686d.
[22] S. Mandal, C. Banerjee, S. Ghosh, J. Kuchlyan, N. Sarkar, Modulation of the photophysical properties of curcumin in nonionic surfactant (Tween-20) forming micelles and niosomes: a comparative study of different microenvironments, The Journal of Physical Chemistry B 117 (23) (2013) 6957–6968, doi:10.1021/jp403724g.
[23] R.K. Saini, K. Das, Picosecond spectral relaxation of curcumin excited state in a binary solvent mixture of toluene and methanol, The Journal of Physical Chemistry B 116 (34) (2012) 10357–10363, doi:10.1021/jp305447y.
[24] K.T. Kazantzis, K. Koutsonikoli, B. Mavroidi, M. Zachariadis, P. Alexiou, M. Pelecanou, M. Sagnou, Curcumin derivatives as photosensitizers in photodynamic therapy: photophysical properties and in vitro studies with prostate cancer cells, Photochemical & Photobiological Sciences 19 (2020) 193–206, doi:10.1039/c9pp00375d.
[25] X. Yang, X. Chen, G. Bian, J. Tu, Y. Xing, Y. Wang, Z. Chen, Proteolytic processing, deubiquitinase and interferon antagonist activities of Middle East respiratory syndrome coronavirus papain-like protease, Journal of General Virology 95 (3) (2014) 614–626, doi:10.1099/vir.0.059014-0.
[26] S.K. Das, S. Mahanta, B. Tanti, H. Tag, P.K. Hui, Identification of phytocompounds from Houttuynia cordata Thunb. as potential inhibitors for SARS-CoV-2 replication proteins through GC–MS/LC–MS characterization, molecular docking and molecular dynamics simulation, Molecular Diversity 26 (1) (2022) 365–388, doi:10.1007/s11030-021-10226-2.

[27] C. Lee, W. Yang, R.G. Parr, Development of the Colle-Salvetti correlation-energy formula into a functional of the electron density, Physical review B 37 (2) (1988) 785, doi:10.1103/Phys.
[28] P.J. Stephens, F.J. Devlin, C.F. Chabalowski, M.J. Frisch, Ab initio calculation of vibrational absorption and circular dichroism spectra using density functional force fields, The Journal of physical chemistry 98 (45) (1994) 11623–11627, doi:10.1021/j100096a001.
[29] A.D. Becke, A new mixing of Hartree–Fock and local density-functional theories, The Journal of chemical physics 98 (2) (1993) 1372–1377, doi:10.1063/1.464304.
[30] S.H. Vosko, L. Wilk, M. Nusair, Accurate spin-dependent electron liquid correlation energies for local spin density calculations: a critical analysis, Canadian Journal of physics 58 (8) (1980) 1200–1211, doi:10.1139/p80-159.
[31] G.W.T.M.J. Frisch, H.B. Schlegel, G.E. Scuseria, M.A. Robb, J.R. Cheeseman, G. Scalmani, V. Barone, G.A. Petersson, H. Nakatsuji, X. Li, M. Caricato, A. Marenich, J. Bloino, B.G. Janesko, R. Gomperts, B. Mennucci, H.P. Hratchian, J.V. Ortiz, A.F. Izmaylov, J.L. Sonnenberg, D. Williams- Young, F. Ding, F. Lipparini, F. Egidi, J. Goings, B. Peng, A. Petrone, T. Henderson, D. Ranasinghe, V.G. Zakrzewski, J. Gao, N. Rega, G. Zheng, W. Liang, M. Hada, M. Ehara, K. Toyota, R. Fukuda, J. Hasegawa, M. Ishida, T. Nakajima, Y. Honda, O. Kitao, H. Nakai, T. Vreven, K. Throssell, J.A. Montgomery Jr., J.E. Peralta, F. Ogliaro, M. Bearpark, J.J. Heyd, E. Brothers, K.N. Kudin, V.N. Staroverov, T. Keith, R. Kobayashi, J. Normand, K. Raghavachari, A. Rendell, J.C. Burant, S.S. Iyengar, J. Tomasi, M. Cossi, J.M. Millam, M. Klene, C. Adamo, R. Cammi, J.W. Ochterski, R.L. Martin, K. Morokuma, O. Farkas, J.B. Foresman, D.J Fox, Gaussian16 Revision A. 03, Gaussian Inc., Wallingford CT, 2016.
[32] P. Galer, A. Golobič, J. Koller, B. Košmrlj, B. Šket, Structures in solid state and solution of dimethoxy curcuminoids: regioselective bromination and chlorination, Chemistry Central Journal 7 (1) (2013) 1–20, doi:10.1186/1752-153X-7-107.
[33] A.D. Bochevarov, E. Harder, T.F. Hughes, J.R. Greenwood, D.A. Braden, D.M. Philipp, D. Rinaldo, M.D. Halls, J. Zhang, R.A. Friesner, Jaguar: A high-performance quantum chemistry software program with strengths in life and materials sciences, International Journal of Quantum Chemistry 113 (18) (2013) 2110–2142, doi:10.1002/qua.24481.
[34] L.D. Jacobson, A.D. Bochevarov, M.A. Watson, T.F. Hughes, D. Rinaldo, S. Ehrlich, R.A. Friesner, Automated transition state search and its application to diverse types of organic reactions, Journal of chemical theory and computation 13 (11) (2017) 5780–5797, doi:10.1021/acs.jctc.7b00764.
[35] Shaw Research, D. E.Maestro-Desmond Interoperability Tools, Schrodinger Release 2023-1, Desmond Molecular Dynamic System, New York, NY, 2021.
[36] E. Harder, W. Damm, J. Maple, C. Wu, M. Reboul, J.Y. Xiang, R.A. Friesner, OPLS3: a force field providing broad coverage of drug-like small molecules and proteins, Journal of chemical theory and computation 12 (1) (2016) 281–296, doi:10.1021/acs.jctc.5b00864.
[37] D. Shivakumar, J. Williams, Y. Wu, W. Damm, J. Shelley, W. Sherman, Prediction of absolute solvation free energies using molecular dynamics free energy perturbation and the OPLS force field, Journal of chemical theory and computation 6 (5) (2010) 1509–1519, doi:10.1021/ct900587b.
[38] W.L. Jorgensen, D.S. Maxwell, J. Tirado-Rives, Development and testing of the OPLS all-atom force field on conformational energetics and properties of organic liquids, Journal of the American Chemical Society 118 (45) (1996) 11225–11236, doi:10.1021/ja9621760.
[39] W.L. Jorgensen, J. Tirado-Rives, The OPLS [optimized potentials for liquid simulations] potential functions for proteins, energy minimizations for crystals of cyclic peptides and crambin, Journal of the American Chemical Society 110 (6) (1988) 1657–1666, doi:10.1021/ja00214a001.
[40] K. Binder, J. Horbach, W. Kob, W. Paul, F. Varnik, Molecular dynamics simulations, Journal of Physics: Condensed Matter 16 (5) (2004) S429, doi:10.1088/0953-8984/16/5/006.
[41] G. Bitencourt-Ferreira, M. Veit-Acosta, W.F. de Azevedo, Hydrogen bonds in Protein-Ligand complexes, Methods in Molecular Biology 2053 (2019) 93–107, doi:10.1007/978-1-4939-9752-7_7.
[42] S. Ghosh, D. Chetia, N. Gogoi, M. Rudrapal, Design, molecular docking, drug-likeness, and molecular dynamics studies of 1, 2, 4-trioxane derivatives as novel Plasmodium falciparum falcipain-2 (FP-2) inhibitors, BioTechnologia. Journal of Biotechnology Computational Biology and Bionanotechnology 102 (3) (2021) 257–275, doi:10.5114/bta.2021.108722.
[43] J.A. Junejo, K. Zaman, M. Rudrapal, I. Celik, E.I. Attah, Antidiabetic bioactive compounds from Tetrastigma angustifolia (Roxb.) Deb and Oxalis debilis Kunth. Validation of ethnomedicinal claim by in vitro and in silico studies, South African Journal of Botany 143 (2021) 164–175, doi:10.1016/j.sajb.2021.07.023.
[44] P.R. Spackman, M.J. Turner, J.J. McKinnon, S.K. Wolff, D.J. Grimwood, D. Jayatilaka, M.A. Spackman, Crystal Explorer: A program for Hirshfeld surface analysis, visualization and quantitative analysis of molecular crystals, Journal of Applied (2021), doi:10.1107/S1600576721002910.
[45] M.A. Spackman, D. Jayatilaka, Hirshfeld surface analysis, CrystEngComm 11 (1) (2009) 19–32, doi:10.1039/B818330A.
[46] A. Parkin, G. Barr, W. Dong, C.J. Gilmore, D. Jayatilaka, J.J. McKinnon, C.C. Wilson, Comparing entire crystal structures: structural genetic fingerprinting, CrystEngComm 9 (8) (2007) 648–652, doi:10.1039/B704177B.
[47] A. Hachani, I. Dridi, S. Elleuch, T. Roisnel, R. Kefi, Crystal structure, spectroscopic and biological study of a new inorganic-organic hybrid compound [Cd4Cl12 (H2O) 2] n (C10N4H28) n, Inorganic Chemistry Communications 100 (2019) 134–143, doi:10.1016/j.inoche.2018.12.006.
[48] K. Selvam, S. Gandhi, S. Krishnamurty, G. Gopalakrishnan, Effect of substitution on the excited state photophysical and spectral properties of boron difluoride curcumin complex dye and their derivatives: A time dependent-DFT study, Journal of Photochemistry and Photobiology B: Biology 199 (2019) 111595, doi:10.1016/j.jphotobiol.2019.111595.
[49] M.K. Sadigh, M.S. Zakerhamidi, A.N. Shamkhali, E. Babaei, Photo-physical behaviors of various active forms of curcumin in polar and low polar environments, Journal of Photochemistry and Photobiology A: Chemistry 348 (2017) 188–198, doi:10.1016/j.jphotochem.2017.08.050.
[50] R.A. Marcus, Electron transfer reactions in chemistry. Theory and experiment, Reviews of Modern Physics 65 (1993) 599–610, doi:10.1103/RevModPhys.65.599.
[51] V. Coropceanu, J. Cornil, D.A. da Silva Filho, Y. Olivier, R. Silbey, J.L. Brédas, Charge transport in organic semiconductors, Chemical reviews 107 (4) (2007) 926–952, doi:10.1021/cr050140x.
[52] S. Armaković, S.J. Armaković, V. Holodkov, S. Pelemiš, Optoelectronic properties of higher acenes, their BN analogue and substituted derivatives, Materials Chemistry and Physics 170 (2016) 210–217, doi:10.1016/j.matchemphys.2015.12.041.
[53] S.J. Armaković, Y.S. Mary, Y.S. Mary, S. Pelemiš, S. Armaković, Optoelectronic properties of the newly designed 1, 3, 5-triazine derivatives with isatin, chalcone and acridone moieties, Computational and Theoretical Chemistry 1197 (2021) 113160, doi:10.1016/j.comptc.2021.113160.
[54] S. Armaković, S.J. Armaković, S. Koziel, Optoelectronic properties of curved carbon systems, Carbon 111 (2017) 371–379, doi:10.1016/j.carbon.2016.10.022.
[55] I. Fleming, Molecular Orbital Theory. In Molecular Orbitals and Organic Chemical Reactions, in: I. Fleming (Ref (Ed.), Molecular Orbitals and Organic Chemical Reactions, John Wiley & Sons, Ltd, 2010, pp. 1–67, doi:10.1002/9780470689493.ch1.
[56] I. Fleming, Molecular Orbitals and the Structures of Organic Molecules. In Molecular Orbitals and Organic Chemical Reactions, in: I. Fleming (Ref (Ed.), Molecular Orbitals and Organic Chemical Reactions, John Wiley & Sons, Ltd, 2010, pp. 69–125, doi:10.1002/9780470689493.ch2.
[57] H. Weinstein, R. Osman, J.P. Green, S. Topiol, Electrostatic Potentials as Descriptors of Molecular Reactivity: The Basis of Some successful Predictions of Biological Activity, in: P. Politzer, D.G. Truhlar (Eds.), Chemical Applications of Atomic and Molecular Electrostatic Potentials, Springer, Boston, MA, 1981, pp. 309–334, doi:10.1007/978-1-4757-9634-6_14.
[58] P. Politzer, J.S. Murray, Quantitative analyses of molecular surface electrostatic potentials in relation to hydrogen bonding and co-crystallization, Crystal Growth & Design 15 (8) (2015) 3767–3774, doi:10.1021/acs.cgd.5b00419.
[59] P. Politzer, J.S. Murray, M.C. Concha, The complementary roles of molecular surface electrostatic potentials and average local ionization energies with respect to electrophilic processes, International journal of quantum chemistry 88 (1) (2002) 19–27, doi:10.1002/qua.10109.
[60] T. Lu, F. Chen, Multiwfn: A multifunctional wavefunction analyzer, Journal of computational chemistry 33 (5) (2012) 580–592, doi:10.1002/jcc.22885.
[61] T. Lu, F. Chen, Quantitative analysis of molecular surface based on improved Marching Tetrahedra algorithm, Journal of Molecular Graphics and Modelling 38 (2012) 314–323, doi:10.1016/j.jmgm.2012.07.004.
[62] C. Ma, M.D. Sacco, Z. Xia, G. Lambrinidis, J.A. Townsend, Y. Hu, J. Wang, Discovery of SARS-CoV-2 papain-like protease inhibitors through a combination of high-throughput screening and a FlipGFP-based reporter assay, ACS central science 7 (7) (2021) 1245–1260, doi:10.1021/acscentsci.1c00519.
[63] D.L. Cramer, B. Cheng, J. Tian, J.H. Clements, R.M. Wypych, S.F. Martin, Some thermodynamic effects of varying nonpolar surfaces in protein-ligand interactions, European journal of medicinal chemistry 208 (2020) 112771, doi:10.1016/j.ejmech.2020.112771.
[64] G.M. Morris, R. Huey, W. Lindstrom, M.F. Sanner, R.K. Belew, D.S. Goodsell, A.J. Olson, AutoDock4 and AutoDockTools4: Automated docking with selective receptor flexibility, Journal of computational chemistry 30 (16) (2009) 2785–2791, doi:10.1002/jcc.21256.
[65] BIOVIA, Dassault Systemes, Biovia Discovery Studio 4, 5, Dassault Systemes, San Diego, 2019.
[66] V. Salmaso, S. Moro, Bridging molecular docking to molecular dynamics in exploring ligand-protein recognition process: An overview, Frontiers in pharmacology 9 (2018) 923, doi:10.3389/fphar.2018.00923.
[67] K. Binder, J. Horbach, W. Kob, W. Paul, F. Varnik, Molecular dynamics simulations, Journal of Physics: Condensed Matter 16 (5) (2004) S429, doi:10.1088/0953-8984/16/5/006.
[68] K. Sargsyan, C. Grauffel, C. Lim, How molecular size impacts RMSD applications in molecular dynamics simulations, Journal of chemical theory and computation 13 (4) (2017) 1518–1524, doi:10.1021/acs.jctc.7b00028.
[69] J.L. Velázquez-Libera, F. Durán-Verdugo, A. Valdés-Jiménez, G. Núñez-Vivanco, J. Caballero, LigRMSD: A web server for automatic structure matching and RMSD calculations among identical and similar compounds in protein-ligand docking, Bioinformatics 36 (9) (2020) 2912–2914, doi:10.1093/bioinformatics/btaa018.
[70] L. Martínez, Automatic identification of mobile and rigid substructures in molecular dynamics simulations and fractional structural fluctuation analysis, PloS one 10 (3) (2015) e0119264, doi:10.1371/journal.pone.0119264.
[71] M.Y. Lobanov, N.S. Bogatyreva, O.V. Galzitskaya, Radius of gyration as an indicator of protein structure compactness, Molecular Biology 42 (2008) 623–628, doi:10.1134/S0026893308040195.

[72] S. Ghosh, D. Chetia, N. Gogoi, M. Rudrapal, Design, molecular docking, drug-likeness, and molecular dynamics studies of 1, 2, 4-trioxane derivatives as novel Plasmodium falciparum falcipain-2 (FP-2) inhibitors, BioTechnologia. Journal of Biotechnology Computational Biology and Bionanotechnology 102 (3) (2021) 257–275, doi:10.5114/bta.2021.108722.

[73] I.M. Othman, M.H. Mahross, M.A. Gad-Elkareem, M. Rudrapal, N. Gogoi, D. Chetia, A. Kadri, Toward a treatment of antibacterial and antifungal infections: design, synthesis and in vitro activity of novel arylhydrazothiazolylsulfonamides analogues and their insight of DFT, docking and molecular dynamic simulations, Journal of Molecular Structure 1243 (2021) 130862, doi:10.1016/j.molstruc.2021.130862.

[74] M. Rudrapal, A.R. Issahaku, C. Agoni, A.R. Bendale, A. Nagar, M.E. Soliman, D. Lokwani, In silico screening of phytopolyphenolics for the identification of bioactive compounds as novel protease inhibitors effective against SARS-CoV-2, Journal of Biomolecular Structure and Dynamics 40 (20) (2022) 10437–10453, doi:10.1080/07391102.2021.1944909.